Article:
Eelen, G, Dubois, C, Cantelmo, AR et al. (36 more authors) (2018) Role of glutamine synthetase in angiogenesis beyond glutamine synthesis. Nature, 561 (7721). pp. 63-69. ISSN 0028-0836

https://doi.org/10.1038/s41586-018-0466-7

ROLE OF GLUTAMINE SYNTHETASE IN ANGIOGENESIS

BEYOND GLUTAMINE SYNTHESIS

Guy Eelen[1-3§], Charlotte Dubois[1,3*], Anna Rita Cantelmo[1,3&], Jermaine Goveia[1,3], Ulrike Brüning[1,3$], Michael DeRan[4], Gopala Jarugumilli[4], Jos van Rijssel[5], Giorgio Saladino[6], Federico Comitani[6], Annalisa Zecchin[1,3], Susana Rocha[7], Rongyuan Chen[2], Hongling Huang[1,3†], Saar Vandekeere[1,3], Joanna Kalucka[1,3], Christian Lange[1,3‡], Francisco Morales-Rodriguez[1,3], Bert Cruys[1,3], Lucas Treps[1,3], Leanne Ramer[1,3#], Stefan Vinckier[1,3], Katleen Brepoels[1,3], Sabine Wyns[1,3], Joris Souffreau[1,3], Luc Schoonjans[1,3], Wouter H. Lamers[8], Yi Wu[9], Jurgen Haustraete[10,11], Johan Hofkens[7], Sandra Liekens[12], Richard Cubbon[1,3,¶], Bart Ghesquière[13], Mieke Dewerchin[1,3], Francesco L. Gervasio[6,14], Xuri Li[2§], Jaap D. van Buul[5], Xu Wu[4] & Peter Carmeliet[1-3§]*

(1) Center for Cancer Biology, University of Leuven, Leuven, B-3000, Belgium; (2) State Key Laboratory of Ophthalmology, Zhongsan Ophthalmic Center, Sun Yat-Sen University, Guangzhou, China; (3) Center for Cancer Biology, VIB, Leuven, B-3000, Belgium; (4) Cutaneous Biology Research Center, Massachusetts General Hospital, Harvard Medical School, Charlestown, Massachusetts 02129, USA; (5) Department of Molecular Cell Biology, Sanquin Research and Landsteiner Laboratory, Academic Medical Centre, University of Amsterdam, 1066CX Amsterdam, the Netherlands; (6) Department of Chemistry, University College London, London WC1E6BT, UK; (7) Molecular Imaging and Photonics, University of Leuven, Leuven, B-3000, Belgium; (8) Tytgat Institute for Liver and Gastrointestinal Research, Academic Medical Center University of Amsterdam, 1105BK Amsterdam, The Netherlands; (9) Center for Cell Analyses and Modelling, University of Connecticut Health Centre, Farmington 06032, USA; (10) Inflammation Research Center, VIB, Ghent, B-9000, Belgium; (11) Department of Biomedical Molecular Biology, Ghent University, Ghent, B-9000, Belgium; (12) Department of Microbiology and Immunology, University of Leuven, Leuven, B-3000, Belgium; (13) Metabolomics Core Facility, Center for Cancer Biology, VIB, Leuven, B-3000, Belgium; (14) Institute of Structural Molecular Biology, University College London, London WC1E6BT, UK. Present affiliations: (&) Université de Lille, INSERM U1003, Physiologie Cellulaire, F-59000 Lille, France; ($) Max-Delbrück-Center for Molecular Medicine, 13092 Berlin, Germany ; (†) Immunology Department, St. Jude Children's Research Hospital, Memphis 38105, USA; (‡) DFG-Research Center for Regenerative Therapies, Technical University Dresden, 01307 Dresden, Germany; (#) Department of Biomedical Physiology and Kinesiology, Simon Fraser University, Burnaby V5A 1S6, Canada; (¶) Division of Cardiovascular and Diabetes Research, Multidisciplinary Cardiovascular Research Centre, University of Leeds, Leeds LS29JT, U.K. *equal contribution; §co-corresponding author

Editorial correspondence: P. Carmeliet & G. Eelen phone: 32-16-373204
e-mail: peter.carmeliet@kuleuven.vib.be

Xuri Li phone: 0086-20-87331815
e-mail: lixr6@mail.sysu.edu.cn

Glutamine synthetase (GS) converts glutamate and NH_4^+ to glutamine. GS is expressed by endothelial cells (ECs), but surprisingly shows negligible glutamine synthesizing activity at physiological glutamine levels. Nonetheless, genetic loss of *GS* in ECs impairs vessel sprouting during vascular development, while pharmacological GS blockade suppresses angiogenesis in ocular and inflammatory skin disease, only minimally affecting healthy adult quiescent ECs. This relies on inhibition of EC migration but not proliferation. Mechanistically, GS knockdown (GS^{KD}) reduces membrane localization and activation of the GTPase RHOJ, while activating other Rho GTPases and Rho kinase (ROCK), thereby inducing actin stress fibers and impeding EC motility. ROCK inhibition rescues the GS^{KD} EC migratory defect. Notably, GS is auto-palmitoylated and interacts with RHOJ to sustain RHOJ palmitoylation, membrane localization and activation. These findings highlight a novel molecular activity for GS, in addition to its glutamine synthesizing activity, in EC migration during pathological angiogenesis.

Endothelial cells (ECs) line the lumen of blood vessels. Emerging evidence reveals that EC metabolism controls vessel sprouting (angiogenesis)[1-3]. While glutamine catabolism in ECs was recently characterized[4], it remains undetermined if glutamine anabolism controls angiogenesis *in vivo*. Glutamine is a carbon and nitrogen donor for biomolecule production and is involved in redox homeostasis. Most cells take up glutamine and thus do not need to synthesize it. Nonetheless, certain cell types express glutamine synthetase (*GS*; also called glutamate-ammonia ligase; *GLUL*), the enzyme capable of *de novo* glutamine production from glutamate and ammonia in an ATP and Mg^{2+}/Mn^{2+} requiring reaction. GS serves also another biochemical function, i.e. ammonia clearance, but this is best described for hepatocytes, astrocytes and muscle. ECs also express GS[5], though its role and importance in angiogenesis remain puzzling, given that ECs are exposed to high plasma glutamine levels. Global *GS* deficiency causes embryonic lethality, presumably

due to the inability to detoxify ammonia[6]. *GS* deficiency in humans is extremely rare and leads to multi-organ failure with infant death[7]. If and how GS affects angiogenesis has never been analyzed. Here we characterized the role and importance of GS in vessel sprouting.

VESSEL SPROUTING REQUIRES ENDOTHELIAL GS

We checked GS expression in endothelial cells of the retinal microvasculature with a genetic *GS* reporter mouse (*GS*$^{+/GFP}$ mice with a nucleus-targeted *GFP-lamin A* fusion reporter transgene in the *GS* ORF of one allele[6]). GFP tracing in the postnatal day 5 (P5) retinal plexus, co-stained with the endothelial cell marker Isolectin B4 (IB4; red), revealed endothelial expression of GFP (and thus of GS) in the microvasculature (Fig. 1a).

Human umbilical venous endothelial cells (further referred to as “ECs”) expressed *GS* to similar levels as human colon ECs, liver ECs, human umbilical arterial ECs and blood outgrowth ECs (BOECs), but to a lower level than lung ECs (Extended Data Fig. 1a). However, GS expression in ECs or isolated mouse liver ECs (mLiECs) was lower than in HEPG2 hepatocellular carcinoma cells or astrocytes (Extended Data Fig. 1a-c), known to highly express GS. Glutamine withdrawal (below physiological concentration of 0.6 mM) increased GS protein levels in ECs (Fig. 1b; Extended Data Fig. 1b), as previously documented for other cell types[8].

We intercrossed *GS*$^{lox/lox}$ mice with two different EC-specific tamoxifen inducible Cre driver lines, i.e. *VE-cadherin(PAC)-Cre*^{ERT2} and *Pdgfb-Cre*^{ERT2} mice to obtain respectively GS^{vECKO} and GS^{pECKO} mice. Correct recombination of the loxed *GS* allele was confirmed (Extended Data Fig. 1d-e) and caused an average 84% reduction of *GS* mRNA levels in mLiECs isolated from GS^{vECKO} mice (Fig. 1c). In the neonatal retina, vascular plexi in P5 GS^{vECKO} mice showed hypobranching and reduced radial expansion, whereas vessel coverage by NG2^{+} pericytes and vessel regression (number of empty collagen IV^{+}

sleeves) were unaffected (Fig.1d-h, Extended Data Fig. 1f,g). However, the number of filopodia at the vascular front and of distal sprouts with filopodia, both parameters of EC migration, was lower in GS^{vECKO} pups (Fig 1i-j). Furthermore, the complexity of the vasculature at the utmost leading front of the plexus was decreased as determined by counting the number of branches in distal sprouts (Extended Data Fig. 1h). In contrast, quantification of $IB4^+$ EdU^+ cells revealed no difference in the number of proliferating ECs (Fig. 1k-m; Extended Data Fig. 1i). Hypobranching was also observed in the dorsal dermal blood vasculature in E16.5 GS^{vECKO} embryos (Fig. 1n-r). A similar retinal phenotype was observed in GS^{pECKO} mice (Extended Data Fig. 1j-m). Thus, loss of endothelial GS causes vascular defects by impairing EC migration but not proliferation.

The retinal vascular defect restored over time (Extended Data Fig. 1n-u) and at 6 weeks, GS^{vECKO} animals (with *GS* deleted in ECs at P1-P3) did not show overt vascular defects (Extended Data Fig. 1v-ag). GS^{vECKO} animals gained normal body weight, and blood biochemistry and hematological profiles were normal at 6 weeks (Extended Data Table 1). Vascular restoration may relate to the possibility that homozygous mutant ECs were outcompeted over time by residual wild type ECs, in which recombination did not occur (as documented in mice with endothelial loss of other key metabolic genes[9]) or because of other compensatory adaptations. Alternatively, the results raise the question if the effect of endothelial GS loss may be larger in growing (motile) ECs during vascular development than in quiescent (non-motile) ECs during adulthood in healthy conditions.

We then explored if pharmacological blockade of GS with methionine sulfoximine (MSO), which irreversibly blocks its catalytic activity, reduced pathological angiogenesis. First, in the oxygen-induced model of retinopathy of prematurity (ROP)[2,3], treatment of pups with MSO reduced the formation of pathological vascular tufts (Fig. 2a-c), while modestly increasing the vaso-obliterated area (Fig. 2d and Extended Data Fig. 1ah-ai). Second, we used the corneal micro-pocket assay (CPA) in mice with slow-release basic fibroblast

growth factor (bFGF) containing pellets as a model of corneal neovascularization. Inclusion of MSO in the pellet reduced formation of new $CD31^+$ blood vessels in the otherwise avascular cornea (Fig. 2e-g). Finally, we used the imiquimod-based mouse model of inflammation-driven skin psoriasis and found a remarkable dose-dependent reduction of the $CD105^+$ EC area upon topical treatment of the affected skin with MSO (Fig. 2h-l). Thus, pharmacological GS blockade inhibits pathological angiogenesis in the inflamed skin and in several eye disorders.

SILENCING GS REDUCES EC MIGRATION

We then used *GS* knockdown (GS^{KD}) ECs (shRNA-mediated; >80% silencing; Extended Data Fig. 2a) in *in vitro* spheroid sprouting assays to assess vessel sprouting. GS^{KD} reduced the number of sprouts per spheroid and the total sprout length (Fig. 3a,b,e,f). Re-introduction of a shRNA resistant *GS* (rGS^{OE}) rescued the sprouting defect (Extended data Fig. 2b-c). The sprouting defect in GS^{KD} spheroids was maintained upon mitotic inactivation of ECs with mitomycin C (MitoC) (Fig. 3c-f), further suggesting an EC motility defect. In agreement, at physiological glutamine levels, GS^{KD} did not affect EC proliferation (Fig. 3g). The sprouting defect was also not due to reduced EC viability or increased oxidative stress, or to changes in energy charge, glutathione or NADPH levels, glycolysis, glucose or glutamine oxidation, or oxygen consumption (Extended Data Fig. 2d-m).

GS^{KD} impaired migration in scratch-wound and Boyden chamber assays, even upon MitoC treatment, an effect that was rescued by re-introducing a shRNA-resistant *GS* (rGS^{OE}) (Fig. 3h-i). Furthermore, sparsely seeded GS^{KD} ECs had a reduced velocity of random movement (Fig. 3j; Supplemental videos 1 and 2) and a decreased lamellipodial area (Fig. 3k-m). Comparable results were obtained with a second non-overlapping shRNA and a *GS*-specific siRNA (Extended Data Fig. 2a; Extended Data Fig. 3a-e).

The migration defects suggested that GS^{KD} perturbed the remodeling of the actin cytoskeleton, necessary for cellular motility. Notably, we detected an increase in F-actin levels in GS^{KD} ECs (Fig. 3n). A role of GS in cytoskeletal remodeling was further suggested by analyzing repolymerization of the actin cytoskeleton upon disruption with the F-actin polymerization inhibitor latrunculin B and subsequent wash-out. Latrunculin B perturbed the normal morphology of control and GS^{KD} ECs (Fig. 3o-r). After wash-out, when control cells had rebuilt a normal actin cytoskeleton, GS^{KD} ECs still had higher F-actin levels, mainly originating from increased numbers of stress fiber bundles (Fig. 3s-u). GS^{KD} did not alter α-tubulin levels (Fig. 3v; Extended data Fig. 4a-h).

The increase in F-actin levels was also present in ECs, freshly isolated from MSO-treated mice (Extended data Fig. 4i-k), and in confluent GS^{KD} ECs aligning a scratch wound *in vitro* (Extended data Fig. 4l-n). Confluent monolayer GS^{KD} ECs displayed compromised junctional integrity (Extended data Fig. 4o-v). Functionally, this corresponded to a decrease in trans-endothelial electrical resistance (TEER) of GS^{KD} ECs *in vitro* (Extended data Fig. 4w) and increased leakiness of inflamed (but not healthy) vessels *in vivo* (Extended data Fig. 4x-z).

GLUTAMINE PRODUCTION BY ENDOTHELIAL GS

To explore whether the migration defect was attributable to reduced *de novo* glutamine synthesis, we measured the glutamine synthesizing activity of GS by supplementing ECs with $^{15}NH_4Cl$ (Extended Data Fig. 5a). At a physiological concentration of 0.6 mM glutamine or higher, the glutamine producing activity of GS was negligible, approximating the level observed in ECs treated with MSO; it slightly increased only upon glutamine withdrawal, presumably to compensate for the lack of available glutamine (Fig. 4a). Similar results were obtained in medium containing dialyzed serum (Extended Data Fig. 5b). For further details see Supplementary Discussion 1 and Extended Data Fig. 5c-n.

To determine if the GS^{KD} phenotype relied on the catalytic site of GS, we used previously reported concentrations of MSO[10], which competes with glutamate in the catalytic site of GS and irreversibly blocks GS. MSO reduced EC spheroid sprouting, impaired EC migration in scratch-wound assays under MitoC treatment, decreased lamellipodial area, while increasing F-actin levels after latrunculin B wash-out but without affecting EC proliferation (Extended Data Fig. 5o-t). Even though other (off-target) effects of pharmacological GS inhibition cannot be formally excluded, MSO phenocopied the *GS* knockdown, suggesting that the catalytic site of GS is indispensable to control EC cytoskeletal homeostasis.

GS INHIBITION AFFECTS RHOJ ACTIVITY

Small GTPases and their effectors control F-actin levels and motility[11], thus we explored if Rho GTPases were downstream targets of GS. We focused on RHOJ, since it is EC-enriched[12], and blocking endothelial RHOJ was proposed to be a novel anti-angiogenesis approach[13]. Of note, $RHOJ^{KD}$ ECs fully phenocopied GS^{KD} ECs in terms of decreased mobility and barrier function (data not shown).

Since RHOJ localizes to plasma and organelle membranes to become activated[14] and RHOJ is almost exclusively detected in the membrane fraction[15], we explored if GS levels regulated RHOJ's membrane localization and activity. Immunoblotting revealed that RHOJ was only detectable in the membrane fraction of ECs (consistent with previous findings[15]), and that GS^{KD} decreased the amount of RHOJ in the membrane fraction (without concomitant increase in the cytosolic fraction, possibly because of proteasomal degradation[16]) as well as the levels of active RHOJ (Fig. 4b,c). GS^{KD} did not overtly affect *RHOJ* transcript levels (relative mRNA levels: 0.99 ± 0.03 in control *vs* 0.85 ± 0.05 in GS^{KD}; n=3, $P = 0.0282$).

We also explored if GS^{KD} affected other Rho GTPases in ECs. We focused on the RHOA/B/C – Rho kinase (ROCK) – myosin light chain (MLC) axis, as silencing of endothelial RHOJ increases signaling of this pathway and induces aberrant F-actin stress fiber formation through an as yet undefined mechanism[13,17] (Fig. 4d). Standard GST-Rhotekin pull-down assays showed that GS^{KD} increased the activity of RHOA and RHOC, but not of RHOB (Fig. 4e-g). Of note, GS^{KD}, much like other stimuli, increased total RHOB levels. We confirmed the increase in RHOA activity at the individual cell level with a DORA-RHOA-FRET biosensor (Fig. 4h; Extended Data Fig. 6a), and observed that the abnormally elevated RHOA activity in retracting lamellipodia in GS^{KD} ECs evoked more numerous, but smaller and more short-lived lamellipodia (Fig. 4i), which could contribute to the motility impairment. As suggested previously[18], increased RHOA activity in lamellipodia locally leads to actomyosin contraction through ROCK and pMLC, thereby prematurely retracting the lamellipodium. Combining GS^{KD} and $RHOJ^{KD}$ did not further increase RHOA activity (data not shown) confirming that RHOJ silencing by itself increased RHOA activity and suggesting that GS indeed primarily acts via RHOJ to control RHOA signaling.

Downstream of Rho GTPases, GS^{KD} and MSO-treated ECs had elevated ROCK1 and ROCK2 protein levels (Fig. 4j), and enhanced ROCK activity, as determined by pMLC protein levels, which were similarly induced in GS^{KD} and $RHOJ^{KD}$ ECs (Fig. 4k; Extended Data Fig. 6b-n). In agreement, ROCK inhibitors (Y27632, fasudil hydrochloride and H1152 dihydrochloride (not shown)) rescued the GS^{KD} phenotype (Fig. 4l-o; Extended Data Fig. 6o-w) whereas myosin light chain kinase (MLCK) inhibitors (ML7; peptide 18) did not (Extended Data Fig. 6x-aa), suggesting that MLC phosphorylation through ROCK rather than MLCK is more important in mediating the GS^{KD} phenotype in ECs. Thus, GS^{KD} lowers membrane localization and activity of RHOJ, while activating RHOA, RHOC, and ROCK.

We explored with which of these Rho GTPases GS interacted, assuming that such an interaction might facilitate / be necessary for their activation, nonetheless keeping in mind that RHOJ can negatively regulate the activity of the RHOA/ROCK/MLC axis[13,17] and hence that loss of a primary interaction of GS with RHOJ could indirectly explain the elevated levels of RHOA/ROCK/MLC upon GS^{KD}. First, co-immunoprecipitation (co-IP) assays showed interaction between endogenous RHOJ and GS (Fig. 5a). Such co-IP was not observed for RHOA and RHOC (most abundant in ECs) (Extended Data Fig. 7a). Second, deletion of the first 20 N-terminal amino acids in RHOJ (ΔN20-RHOJ), mediating RHOJ's plasma membrane localization[19], reduced the interaction with GS (Extended data Fig. 7b). Third, immunoblotting showed that only RHOJ, but not RHOA or RHOC, was predominantly membrane localized (Extended data Fig. 7c). Fourth, we confirmed the GS-RHOJ interaction with a bimolecular fluorescence complementation approach (BiFC) (Extended Data Fig. 7d,e). Based on the above data, we focused on RHOJ as most likely interacting partner of GS.

To interact with membrane-localized (active) RHOJ, GS should be membrane localized as well. Indeed, cell fractionation studies revealed that a fraction of GS was membrane localized (Fig. 5b). Further evidence derives from single particle tracking data, acquired by photoactivated localization microscopy imaging (SPT-PALM), combined with total internal reflection fluorescence microscopy (TIRF). We traced the movement of single GS proteins tagged with the photoswitchable fluorescent protein (PSFP) mEOS (GS-mEOS). Single GS-mEOS particles had a lower diffusion coefficient (DF) in the TIRF region (comprising the plasma membrane and the immediately adjacent cytoplasm) than free mEOS, indicative of an association of GS with membrane structures (Fig. 5c; Extended Data Fig. 7f).

PALMITOYLATION OF GS AND RHOJ

Membrane localization often requires post-translational palmitoylation. We thus hypothesized that GS could be palmitoylated to allow plasma membrane localization and interaction with RHOJ. Therefore, we performed click chemistry with biotin-azide (Extended Data Fig. 7g) on lysates from HEK293 cells overexpressing GS and treated with the clickable palmitoylation probes 16C-BYA or 16C-YA. Streptavidin pull-down showed clear palmitoylation of GS, as both probes labeled GS. The labeling was reduced by MSO, consistent with the presumed dependency of the phenotype on the enzyme's catalytic site (Fig. 5d).

GS was anecdotally reported previously to be palmitoylated, however without further in-depth molecular / functional characterization[20]. To determine if GS undergoes autopalmitoylation, we incubated purified GS[21] with palmitoyl-alkyne CoA (a substrate for palmitoylation) in a cell-free system without any other proteins present, to demonstrate a direct effect. Click chemistry revealed that increasing the dose of palmitoyl-alkyne CoA resulted in increased autopalmitoylation of GS (Fig. 5e). Importantly, autopalmitoylation of GS was achieved with physiological concentrations of palmitoyl-CoA (1-10 μM) at neutral pH, suggesting physiologically relevant autopalmitoylation and was confirmed with two alternative methods (Supplementary Discussion 2 and Extended Data Fig. 7h-j).

Palmitoylation of target proteins by palmitoyl-acyl transferases (PATs) is a two-step reaction, requiring first autopalmitoylation of the PAT, and thereafter, transfer of the palmitoyl group to the target protein. We hypothesized GS to have a similar activity profile (Supplementary Discussion 3) and explored if GS was involved in palmitoylation of RHOJ. Even though RHOJ's cysteines at position 3 (C3) and 11 (C11) were *in silico* predicted to be high fidelity palmitoylation sites (screened with SwissPalm[22], data not shown), palmitoylation of RHOJ has been poorly documented (except in a few studies[23,24]). Interestingly, RHOJ's membrane localization and activity were reduced by treatment of ECs with the pan-palmitoylation inhibitor 2-bromopalmitate (2BP) and by point mutating

cysteines C3 and C11 (Fig. 5f; Extended Data Fig. 7k-t), providing initial evidence that RHOJ can be palmitoylated in ECs. Using the palmitoylation probe 17-ODYA (Fig. 5g) or an acyl-resin-assisted capture (acyl-RAC; Extended Data Fig. 7u), we found a reduction in the levels of palmitoylated RHOJ upon blocking GS, consistent with a model whereby GS sustains palmitoylation of RHOJ.

DISCUSSION

Surprisingly, we found a glutamine synthesizing-independent activity for GS in regulating EC motility, even though we cannot formally exclude a possible contribution of minimal levels of glutamine production by GS to the observed phenotype. Indeed, GS regulates RHOJ signaling in cell motility as shown by several lines of evidence. First, a fraction of GS is present in EC membranes, where active RHOJ resides. Second, GS interacts with RHOJ in ECs in co-IP experiments (though this interaction can be direct / indirect). Third, GS^{KD} reduces RHOJ's palmitoylation, membrane localization and activity in ECs. Thus, since RHOJ promotes EC motility[13,17], the impaired migration of GS^{KD} ECs could be attributed to the reduced RHOJ activity. RHOJ likely also indirectly contributes to promoting EC motility through controlling the activity of the RHOA/ROCK/MLC signaling pathway, known to regulate EC motility by affecting stress fiber formation[13,17] (Extended Data Fig. 7v; Supplementary Discussion 4).

Because purified GS seems capable of autopalmitoylation (a trademark of PAT enzymes), and GS silencing lowers RHOJ palmitoylation, our data support a model, whereby GS first autopalmitoylates itself and thereafter transfers the palmitoyl group to RHOJ, though we cannot formally exclude that transfer of the palmitoyl group from GS to RHOJ occurs via additional partners or even non-enzymatically. A possible model for GS palmitoylation is

described in Supplementary Discussion 5, Extended Data Fig. 8 and Extended Data Table 2. Also, whether the GS-RHOJ partnership is exclusive or GS interacts with other players (*eg* other palmitoylated RhoGTPases such as RAC1, CDC42, RHOU or RHOV) to mediate this effect on EC motility, remains outstanding. In any case, RHOJ seems to be a critical target of GS, given that its silencing completely phenocopies GS inhibition in ECs.

Finally, GS is critical for EC motility / migration, contributing to the formation of new vessels in development and disease. In contrast, ECs do not migrate when they are quiescent in healthy adults, explaining why GS inhibition has no observable effects on the vasculature in healthy adult mice. This renders GS an attractive disease-restricted target for therapeutic inhibition of pathological angiogenesis. In agreement, the pharmacological GS blocker MSO reduced pathological angiogenesis in blinding eye and psoriatic skin disease (Fig. 2), which warrants further exploration of GS targeting in anti-angiogenesis.

REFERENCES

1 De Bock, K. *et al.* Role of PFKFB3-Driven Glycolysis in Vessel Sprouting. *Cell* **154**, 651-663, doi:10.1016/j.cell.2013.06.037 (2013).

2 Schoors, S. *et al.* Fatty acid carbon is essential for dNTP synthesis in endothelial cells. *Nature* **520**, 192-197, doi:10.1038/nature14362 (2015).

3 Schoors, S. *et al.* Partial and transient reduction of glycolysis by PFKFB3 blockade reduces pathological angiogenesis. *Cell Metab* **19**, 37-48, doi:10.1016/j.cmet.2013.11.008 (2014).

4 Huang, H. *et al.* Role of glutamine and interlinked asparagine metabolism in vessel formation. *EMBO J* **36**, 2334-2352, doi:10.15252/embj.201695518 (2017).

5 Abcouwer, S. F., Lukascewicz, G. C., Ryan, U. S. & Souba, W. W. Molecular regulation of lung endothelial glutamine synthetase expression. *Surgery* **118**, 325-334; discussion 335 (1995).

6 He, Y., Hakvoort, T. B., Vermeulen, J. L., Lamers, W. H. & Van Roon, M. A. Glutamine synthetase is essential in early mouse embryogenesis. *Dev Dyn* **236**, 1865-1875, doi:10.1002/dvdy.21185 (2007).

7 Haberle, J. *et al.* Congenital glutamine deficiency with glutamine synthetase mutations. *N Engl J Med* **353**, 1926-1933, doi:10.1056/NEJMoa050456 (2005).

8 Kung, H. N., Marks, J. R. & Chi, J. T. Glutamine synthetase is a genetic determinant of cell type-specific glutamine independence in breast epithelia. *PLoS Genet* **7**, e1002229, doi:10.1371/journal.pgen.1002229 (2011).

9 Schoors, S. *et al.* Incomplete and transitory decrease of glycolysis: a new paradigm for anti-angiogenic therapy? *Cell Cycle* **13**, 16-22, doi:10.4161/cc.27519 (2014).

10 Dadsetan, S. *et al.* Brain alanine formation as an ammonia-scavenging pathway during hyperammonemia: effects of glutamine synthetase inhibition in rats and astrocyte-neuron co-cultures. *J Cereb Blood Flow Metab* **33**, 1235-1241, doi:10.1038/jcbfm.2013.73 (2013).

11 Ridley, A. J. Rho GTPase signalling in cell migration. *Curr Opin Cell Biol* **36**, 103-112, doi:10.1016/j.ceb.2015.08.005 (2015).

12 Yuan, L. *et al.* RhoJ is an endothelial cell-restricted Rho GTPase that mediates vascular morphogenesis and is regulated by the transcription factor ERG. *Blood* **118**, 1145-1153, doi:10.1182/blood-2010-10-315275 (2011).

13 Kim, C. *et al.* Vascular RhoJ is an effective and selective target for tumor angiogenesis and vascular disruption. *Cancer Cell* **25**, 102-117, doi:10.1016/j.ccr.2013.12.010 (2014).

14 Leszczynska, K., Kaur, S., Wilson, E., Bicknell, R. & Heath, V. L. The role of RhoJ in endothelial cell biology and angiogenesis. *Biochem Soc Trans* **39**, 1606-1611, doi:10.1042/BST20110702 (2011).

15 de Toledo, M. *et al.* The GTP/GDP cycling of rho GTPase TCL is an essential regulator of the early endocytic pathway. *Mol Biol Cell* **14**, 4846-4856, doi:10.1091/mbc.E03-04-0254 (2003).

16 Nethe, M. & Hordijk, P. L. The role of ubiquitylation and degradation in RhoGTPase signalling. *J Cell Sci* **123**, 4011-4018, doi:10.1242/jcs.078360 (2010).

17 Kaur, S. *et al.* RhoJ/TCL regulates endothelial motility and tube formation and modulates actomyosin contractility and focal adhesion numbers. *Arterioscler Thromb Vasc Biol* **31**, 657-664, doi:10.1161/ATVBAHA.110.216341 (2011).

18 Heasman, S. J. & Ridley, A. J. Multiple roles for RhoA during T cell transendothelial migration. *Small GTPases* **1**, 174-179, doi:10.4161/sgtp.1.3.14724 (2010).

19 Ackermann, K. L., Florke, R. R., Reyes, S. S., Tader, B. R. & Hamann, M. J. TCL/RhoJ Plasma Membrane Localization and Nucleotide Exchange Is Coordinately Regulated by Amino Acids within the N Terminus and a Distal Loop Region. *J Biol Chem* **291**, 23604-23617, doi:10.1074/jbc.M116.750026 (2016).

20 Wan, J. *et al.* Tracking brain palmitoylation change: predominance of glial change in a mouse model of Huntington's disease. *Chem Biol* **20**, 1421-1434, doi:10.1016/j.chembiol.2013.09.018 (2013).

21 Levine, R. L., Oliver, C. N., Fulks, R. M. & Stadtman, E. R. Turnover of bacterial glutamine synthetase: oxidative inactivation precedes proteolysis. *Proc Natl Acad Sci U S A* **78**, 2120-2124 (1981).

22 Blanc, M. *et al.* SwissPalm: Protein Palmitoylation database. *F1000Res* **4**, 261, doi:10.12688/f1000research.6464.1 (2015).

23 Roberts, P. J. *et al.* Rho Family GTPase modification and dependence on CAAX motif-signaled posttranslational modification. *J Biol Chem* **283**, 25150-25163, doi:10.1074/jbc.M800882200 (2008).

24 Wei, X., Song, H. & Semenkovich, C. F. Insulin-regulated protein palmitoylation impacts endothelial cell function. *Arterioscler Thromb Vasc Biol* **34**, 346-354, doi:10.1161/ATVBAHA.113.302848 (2014).

Supplementary Information is linked to the online version of the paper at www.nature.com/nature.

ONLINE CONTENT

Methods and associated references, and Extended Data display items are available in the online version of the paper.

ACKNOWLEDGMENTS

We acknowledge Rod Levine for supplying purified bacterial GS, Ludo Van Den Bosch and Wendy Scheveneels for providing primary mouse astrocytes, Sander Trenson, Inne Crèvecoeur, Sam Noppen, Lizette Van Berckelaer and Ria Van Berwaer for technical assistance, Sarah-Maria Fendt, Dries Verdegem and Chris Ulens for discussions and suggestions, Wesley Vermaelen, Abel Acosta Sanchez, Aleksandra Brajic, Agua Sobrino and Maaike Cockx for experimental assistance, Lena-Christin Conradi, Andreas Pircher for supplying materials and Els Wauters, Albert Wolthuis and Joris Jaekers for providing tissues for EC isolations. HecBioSim and PRACE are acknowledged for allocation of computer time. JG, ARC, CD, CL, JK, FJMR, SR and SV are supported by the FWO; AZ by LE&RN/FDRS; BC by IWT; UB by a Marie Curie-IEF Fellowship; HH by an EMBO longterm fellowship; JDvB by a LSBR fellowship; RC by a British Heart Foundation Intermediate Clinical Fellowship; and XW by the American Cancer Society RSG, NIH/NCI and NIH/NIDDK. FC, GS and FLG are supported by EPSRC; XL by the State Key Laboratory of Ophthalmology, Zhongshan Ophthalmic Center at Sun Yat-Sen University, and the National Natural Science Foundation of China (81330021 and 81670855). PC is supported by a Federal Government Belgium grant, long-term structural Methusalem funding by the Flemish Government, a Concerted Research Activities Belgium grant, grants from the FWO, Foundation against Cancer and ERC Advanced Research Grant. GE and MD received a Foundation against Cancer grant and GE received a FWO 'Krediet aan navorsers'.

AUTHOR CONTRIBUTIONS

Study concept and supervision: PC; *contribution to the execution, support and analysis of experiments, and/or advice*: GE, PC, XL, MD, LS; *experimental design*: GE, CD, ARC, JG and PC*; molecular biology and* in vivo *experiments*: GE, CD, ARC, JG, UB, AZ, HH, SVa,

JK, CL, FMR, BC, LR, SVi, KB, SW, JS, LS, SL, RCh, RCu, MD; *mass spectrometry*: BG; *RHO activity assays*: JvR, JDvB; GS *palmitoylation*: MDR, GJ, XW; *molecular dynamics simulations*: GS, FC, FLG; *BiFC and SPT*: SR, JHo; *data interpretation*: GE, CD, ARC, JG, RC, UB, CL, SR, LT, BC, MD, JHo, SL, BG, FLG, JDvB, XW and PC; *providing necessary materials*: WHL, YW and JHa; *manuscript drafting*: GE and PC. All authors agreed on the final version of the manuscript.

AUTHOR INFORMATION

The authors declare no competing interests.

Correspondence and requests for materials should be addressed to PC (peter.carmeliet@kuleuven.vib.be).

LEGENDS TO FIGURES

FIGURE 1: EC-SPECIFIC DELETION OF GS CAUSES VASCULAR DEFECTS *IN VIVO*

a, GS expression (arrowheads) in the retinal microvasculature (co-stained with isolectin B4 (IB4)) of five day-old (P5) chimeric $GS^{+/GFP}$ pups (with zoom-in inset). **b,** GS protein levels in HUVECs under different extracellular glutamine levels. **c,** *GS* mRNA levels upon activation of VE-cadherin-Cre^{ERT2}. **d-g,** IB4 staining of P5 retinal vascular plexi from WT (d) and GS^{vECKO} (e) mice (with zoom-in insets, A=artery, V=vein) and quantification of branch points at the front of the plexus (f) and radial expansion of the plexus (g). **h,** Vessel regression (area of collagen IV (Col IV)$^+$ IB4$^-$ vessel sleeves (% of total Col IV$^+$ area)) in retinas from P5 WT and GS^{vECKO} pups. **i-j,** Distal sprouts (i) and filopodia (j) at the retinal vascular front. **k-m,** IB4 (gray)/EdU (cyan) double staining of P5 WT (l) and GS^{vECKO} (m) retinas (arrowheads in zoom-in insets denote EdU$^+$ ECs) and quantification (k) of EdU$^+$ ECs at the front of the plexus. **n-r,** CD31-stained dermal dorsal blood vasculature in E16.5 WT (n,o) and GS^{vECKO} (p,q) mice with boxed regions magnified in (o) and (q) and quantification of number of branch points (r). All data are mean±s.e.m; n-number (individual experiments) is 2 (a,b); n-numbers (individual mice) for WT and GS^{vECKO} are: 3 and 3 (c); 11 and 10 (f); 10 and 7 (g); 4 and 6 (h); 18 and 22 (i); 17 and 21 (j); 12 and 22 (k); 5 and 15 (r), from 2 (g,h,r), 3 (f) or 4 (i,j,k) litters. $^{NS}P>0.05$, $^{*}P<0.05$ according to Student's *t* test (c,g,h,i,j,k,r) or mixed models R statistics (f). Exact *P* values: (c) 0.0215; (f) 0.0141; (g) 0.0063; (h) 0.4902; (i) 0.0009; (j) 0.0484; (k) 0.3837; (r) 0.0046. Scale bars: 10 μm (a right), 50 μm (a left), 100 μm (l,m), 200 μm (d,e,n,p). Gel source images: see Supplemental Information Fig. 1.

FIGURE 2: GS INHIBITION MITIGATES PATHOLOGICAL ANGIOGENESIS

a-d, Retinal flat-mounts of retinopathy of prematurity (ROP) mice treated with vehicle (a) or 20 mg kg^{-1} d^{-1} MSO (b). Quantification of vascular tuft (c) and vaso-obliterated area (d) in control and MSO-treated ROP pups. **e-g,** Quantification (e) of $CD31^{+}$ (green) neo-vessels in corneal flat-mounts from mice in corneal pocket assays (CPA) with bFGF pellets (demarcated by dotted white line) with vehicle (f) or MSO (g). **h-l,** CD105 staining of untreated skin (h), IMQ-treated skin (i), IMQ + low dose MSO-treated skin (j), IMQ + high dose MSO-treated skin (k), and quantification of $CD105^{+}$ area (l). All data are mean±s.e.m.; n-numbers (individual mice) for control and MSO-treated are: 7 and 6 (c,d), 10 and 11 (e) from 3 litters (c,d) and 2 experiments (e). In (l) n=15 for control, n=22 for IMQ, n=18 for IMQ + MSO low (indicated by +) and n=6 animals for IMQ + MSO high (indicated by ++) from 3 experiments. $^{NS}P>0.05$, $^{*}P<0.05$ according to Student's *t* test (c,d,e) or ANOVA with Dunnett's multiple comparisons *vs* IMQ (l). Exact *P* values (c) 0.0459; (d) 0.0145; (e) <0.0001; (l) ctrl *vs* IMQ: 0.0278; MSO low *vs* IMQ: 0.7283; MSO high *vs* IMQ: 0.0451. bFGF: basic fibroblast growth factor; CD31: cluster of differentiation 31; IMQ: imiquimod; MSO: methionine sulfoximine. Scale bars: 100 µm (a,b), 200 µm (f,g), 75 µm (h-k).

FIGURE 3: LOSS OF *GS* IMPAIRS EC MIGRATION THROUGH PERTURBED ACTIN DYNAMICS

a-f, Control (a,c) and GS^{KD} (b,d) EC spheroids without (a,b) and with mitomycin C (MitoC) (c,d) treatment and number of sprouts per spheroid (e) and total sprout length (f). **g,** [^{3}H]-Thymidine incorporation in control and GS^{KD} ECs. **h,** Wound closure upon MitoC-treatment of control and GS^{KD} ECs. **i,** Boyden chamber migration for control, GS^{KD} and GS^{KD} + rGS^{OE} (overexpression of a shRNA-resistant *GS* mutant) ECs, all under MitoC-treatment.

j, Velocity of sparsely seeded control and GS^{KD} ECs. **k-m,** Phalloidin (F-actin) staining of control (k) and GS^{KD} (l) ECs (arrows and white dotted lines indicate lamellipodia) and quantification of lamellipodial area (m). **n-p,** F-actin and G-actin levels in phalloidin (F-actin) – DNAse I (G-actin) double-stained control and GS^{KD} ECs (n), and representative images of phalloidin-stained control (o) and GS^{KD} (p) ECs. **q-u,** Phalloidin staining of latrunculin B-treated control (q,s) and GS^{KD} (r,t) ECs at timepoint 0 (q,r) and at 1 h after latrunculin wash-out (s,t) and quantification of F-actin levels after wash-out (u). **v,** α-Tubulin levels in GS^{KD} and control ECs. All data are mean±s.e.m.; n-numbers (independent experiments) are: 4 (e,f), 9 (g,j), 5 (h), 6 (i,u), 7 (m) and 3 (n,v). $^{NS}P>0.05$, $^{*}P<0.05$ according to mixed models R statistics (e,f), Student's *t* test (g,h,j,m,n,u,v) or ANOVA with Dunnett's multiple comparison *vs* control (i). Exact *P* values (e,f) ctrl *vs* GS^{KD} ± mitoC: <0.0001; (g) 0.7729; (h) 0.0283; (i) ctrl *vs* GS^{KD}: 0.0093; ctrl *vs* GS^{KD} + rGS^{OE}: 0.5981; (j) 0.0234; (m) 0.0352; (n) F-actin: 0.0467; G-actin: 0.584; (u) 0.0007; (v) 0.3491. AU, arbitrary units. Scale bars: 100 µm (a-d), 10 µm (k,l) and 20 µm (o-t).

FIGURE 4: ENDOTHELIAL GS REGULATES RHOGTPASE ACTIVITY

a, Effect of glutamine and MSO on glutamine-producing activity (% enrichment in m+1 glutamine and glutamate, 30 min after adding $^{15}NH_4^+$). **b,** RHOJ, NaK ATPase (membrane marker) and GAPDH (cytosol marker) immunoblots in cytosolic (c) and membrane (m) fractions with quantification **c,** Immunoblot for active and total RHOJ with quantification ($RHOJ^{KD}$, beads only and irrelevant biotinylated peptide are negative controls) **d,** RHOJ's pivotal yet incompletely understood (question mark) role in EC migration/stress fiber formation. **e-g,** Immunoblots for pull-down RHOA (e), RHOB (f) and RHOC (g) activity assays with quantifications. **h,** Control and GS^{KD} ECs expressing the DORA RHOA biosensor, with quantification of whole-cell FRET startratio (mean±s.e.m.; control, n=12 cells; GS^{KD}, n=9). Look-up table (LUT; color bar) denotes relative RHOA activities

(blue=low, red=high). **i,** Kymograph of DORA RHOA biosensor expressing ECs, showing abnormally short-lived lamellipodia and increased RHOA activity in retracting lamellipodia of GS^{KD} ECs (red arrowheads) (representative of 13 control and GS^{KD} cells). **j,** ROCK1, ROCK2, α-tubulin immunoblots with quantification. **k,** pMLC, total MLC and α-tubulin immunoblots (quantification see Methods section). **l,** F-actin levels after latrunculin B wash-out in ECs treated with the ROCK inhibitor Y27632. **m-o,** Effect of Y27632 on spheroid sprouting defect (m), migration defect (n), and lamellipodial area (o). Values in l,n,o are relative to untreated non-silenced control (dotted line). pMLC: phosphorylated MLC. Scale bar is 25 µm (h). All data are mean±s.e.m.; n-numbers (independent experiments) are: 3 (a,e,f,m,n), 4 (c(MSO),h,k,l), 5 (o), 7 (j), 8 (c(GS^{KD}), g), 13 (b). $^{NS}P>0.05$, $^{\#}P=0.05$, $^{*}P<0.05$; ANOVA with Dunnett's multiple comparisons *vs* 4 mM (a), one sample *t* test (b,c,e,f,g,j,k), Student's *t* test (h,n,o), paired Student's *t* test (l) or mixed models R statistics (m). Exact *P* values (a) (Glu) 0.6 mM *vs* 4 mM: 0.9903; 0.025 mM + MSO *vs* 4 mM: 0.0968; 0.025 mM *vs* 4 mM: 0.1943; (Gln) 0.6 mM *vs* 4 mM: 0.4518; 0.025 mM + MSO *vs* 4 mM: 0.9999; 0.025 mM *vs* 4 mM: 0.0143; (b) 0.0072; (c) MSO: 0.0323; GS^{KD}: 0.0095; (e) 0.053; (f) 0.1790; (g) 0.0035; (h) 0.0055; (j) ROCK1 MSO: 0.0169; ROCK1 GS^{KD}: 0.0138; ROCK2 MSO: 0.0381; ROCK2 GS^{KD}: 0.0802; (k) MSO: 0.0283; GS^{KD}: 0.0431; $RHOJ^{KD}$: 0.0091; (l) 0.0431; (m) GS^{KD} *vs* ctrl: <0.0001; GS^{KD} + Y27632 *vs* ctrl + Y27632: 0.5211; (n) 0.0181; (o) 0.0210. Gel source images: see Supplemental Information Fig. 1.

FIGURE 5: GS (AUTO)-PALMITOYLATION

a, Co-immunoprecipitation (Co-IP) of endogenous RHOJ and GS in ECs. Upper panel: IP of RHOJ; lower panel: IP for GS. **b,** Immunoblot for GS and RHOJ in cytosolic (c) and membrane (m) fractions in ECs with NaK and GAPDH as fraction markers. **c,** Diffusion coefficient (DF, in $\mu m^2 s^{-1}$) of single photoswitchable fluorescent protein mEOS and mEOS-

fused GS (mEOS-GS) particles in the plasma membrane region of ECs acquired by SPT-PALM under TIRF illumination (n=41 cells expressing mEOS and 37 expressing mEOS-GS) **d,** GS immunoblotting after streptavidin pull-down of biotin-azide clicked lysates from HEK-293T cells for the indicated palmitoylation probes. Input shows levels of GS overexpression. **e,** Dose-effect of palmitoyl-alkyne CoA on autopalmitoylation of purified GS; biotin-azide clicking and HRP-streptavidin blotting; input on Coomassie-stained gel. **f,** Immunoblotting for RHOJ, NaK and GAPDH in membrane (m) and cytosolic (c) fractions of control- and 2BP-treated ECs. **g,** Palmitoylation of RHOJ in GS^{KD}, MSO- and 2BP-treated ECs. In-gel fluorescence for TAMRA-azide 17-ODYA (palmitoylation probe)-clicked FLAG-RHOJ is shown (FLAG as loading control). 2BP, 2-bromopalmitate, pan-palmitoylation inhibitor. All data are mean±s.e.m., except box and whisker (running from minimal to maximal values) plots in (c); n-numbers (independent experiments) are: 2 (e), 3 (a,b,c,d,f), 4(g). $^{NS}P>0.05$, $^{*}P<0.05$; Student's *t* test (c); one sample *t* test (f,g). Exact *P* values (c) <0.0001; (f) 0.0264; (g) MSO: 0.0317; GS^{KD}: 0.0003; 2BP: 0.0163. Gel source images: see Supplemental Information Fig. 1.

METHODS

CHEMICALS AND REAGENTS: The GS inhibitor L-methionine sulfoximine (MSO), mitomycin C, latrunculin B, oligomycin, antimycin A, carbonyl cyanide-4-(trifluoromethoxy) phenylhydrazone (FCCP), 2-bromohexadecanoic acid (2-bromopalmitic acid, 2BP), tamoxifen, palmitoyl-CoA agarose and α-ketoglutarate dehydrogenase were from Sigma-Aldrich. 17-Octadecynoic acid (17-ODYA) was purchased from Cayman Chemical. The use and/or synthesis of the other palmitoylation probes 15-hexadecynoic acid (16C-YA; a palmitate-based probe that binds a broader spectrum of proteins than 16C-BYA (here below), including both PATs and PAT target proteins) and 2-bromooctadec-15-yonic acid (16C-BYA; a 2-bromopalmitate-based activity-based probe that labels but also inhibits palmitoyl acyltransferase (PAT) enzymes) has been described previously[25]. The ROCK kinase inhibitor Y27632 ((1R,4r)-4-((R)-1-aminoethyl)-N-(pyridin-4-yl)cyclohexanecarboxamide) was from BioVision, fasudil hydrochloride and H1152 dihydrochloride are from Tocris. The MLCK inhibitors ML7-hydrochloride and peptide 18 were from Tocris. Collagen type 1 (rat tail) was obtained from Merck Millipore. [5-^{3}H]-glucose, [^{3}H]-thymidine, [U-^{14}C]-glutamine were from Perkin Elmer; [6-^{14}C]-D-glucose was from ARC. [U-^{13}C]-glucose, [U-^{13}C]-glutamine, [U-^{13}C]-glutamate and $^{15}NH_4Cl$ were purchased from Cambridge Isotope Laboratories. The following primary antibodies or dyes were used (dilutions for staining (ST), immunoblotting (IB), immunofluorescence (IF) and immunoprecipitation (IP) are given in between brackets): *Griffonia simplicifolia* (GS)-IB_4-Alexa 488 (ST 1:200), isolectin GS-IB_4-Alexa 568 (ST 1:200), isolectin GS-IB_4-Alexa 647 (ST 1:200), phalloidin-Alexa 488 (ST 1:100), deoxyribonuclease I-Alexa 594 (ST 1:200) (Molecular Probes), anti-collagen IV (2150-1470) (IF 1:400) (Bio Rad), anti-NG2

Chondroitin Sulfate Proteoglycan (AB5320) (IF 1:200) (Millipore), anti-FLAG (clone M2) (IB 1:1,000; IP 5 μg ml^{-1}), anti-GS (clone 2B12) (IB 1:1,000; IP 2-5 μg ml^{-1}), anti-RHOJ (clone 1E4) (IB 1:1,000; IP 2-5 μg ml^{-1}), anti-ROCK1 (HPA007567) (IB 1:1,000), anti-α-tubulin (T6199) (IB 1:1,000) (Sigma-Aldrich), anti-β-actin (13E5) (IB 1:1,000), anti-phospho-Myosin Light Chain 2 (IB 1:1,000; IF 1:300) and anti-Myosin Light Chain 2 (IB 1:1,000) (9776), anti-Na,K-ATPase (NaK) (3010) (IB 1:1,000), anti-RHOA (67B9) (IB 1:1,000) and anti-RHOC (D40E4) (IB 1:1,000) (Cell Signaling Technology), anti-CD105/endoglin (AF1320) (IF 1:50), anti-VE-cadherin (AF1002) (IF 1:50) (R&D Systems), anti-ROCK2 (A300-047A-T) (IB 1:500) (Imtec Diagnostics), anti-CD31 (MEC13.3) (IF 1:200), anti-CD34-biotin (#553732) (IF 1:25) (BD Biosciences), anti-RHOB (sc-180) (IB 1:1,000). Secondary Alexa-405, -488, -568 or -647 conjugated antibodies (1:500) were from Molecular Probes; other secondary antibodies and IgG controls were from Dako. The Click-iT® 5-ethynyl-2′-deoxyuridine (EdU) Alexa Fluor® 555 Imaging Kit was from Invitrogen. Purified bacterial GS was a kind gift from Rod Levine (Bethesda, MD, USA).

CELL CULTURE: *HUMAN UMBILICAL VEIN ENDOTHELIAL CELLS (HUVECS) AND HUMAN UMBILICAL ARTERY ENDOTHELIAL CELLS (HUAECS)* obtained under protocol S57123 (Commission Medical Ethics of UZ/KU Leuven) after written consent of the donors, were isolated as previously described [1,2] and were routinely cultured in M199 medium (Invitrogen) containing 20% FBS, 0.6 mM L-glutamine, heparin (10 U ml^{-1}; Sigma), penicillin (100 U ml^{-1}), streptomycin (100 μg ml^{-1}) and endothelial cell growth factor supplements (EGCS; 30 mg l^{-1}; Sigma). Cells were only used between passages 1 and 4 and all experiments were performed in HUVECs from at least three different donors unless stated otherwise. Also except when stated otherwise, the use of the abbreviation EC in the text refers to HUVEC. *ISOLATION OF ENDOTHELIAL CELLS FROM HUMAN LUNG/LIVER/COLON MUCOSA*: Lung/liver/colon mucosa specimens were obtained under protocol S57123 (Commission Medical Ethics of UZ/KU Leuven) and were washed several times with phosphate buffer solution (PBS) and

minced with scissors prior to enzymatic digestion for 45 min. at 37 °C with collagenase/dispase/DNase solution (Gibco, Life Technologies). The resulting suspension was passed through a 100 μm nylon mesh (BD Biosciences Pharmingen) to remove aggregates. The harvested cells were washed, seeded on gelatin pre-coated 6-well plates and cultured in complete endothelial growth medium (EGM-MV; Lonza) supplemented with antibiotics. After 5-7 days, when cells reached confluency, a positive CD31 magnetic bead selection was performed (CD31 MicroBead, #130-091-935, Miltenyi Biotech) according to the manufacturer's guidelines and purified cells were further cultured in EGM medium. *PERIPHERAL BLOOD OUTGROWTH ENDOTHELIAL CELLS (BOECS)* were established and cultured as previously described [26]. In brief, blood samples (obtained under protocol S57123 (Commission Medical Ethics of UZ/KU Leuven) were diluted with PBS prior to Ficoll PaquePLUS (GE Healthcare) density-gradient centrifugation at 1,000 g for 20 min at room temperature. The mono-nuclear cell layer was collected, washed with PBS and resuspended in EGM2 medium (PromoCell). Cells were plated in collagen-coated flasks and medium was replaced every 2 days. From day 7 onwards, cells were checked for the formation of colonies, which were allowed to grow up to approximately 1 cm^2. BOEC colonies were then trypsinized and subcultured. *HEK293T AND HEPG2* CELLS (ATCC) were grown in DMEM, supplemented with 10% fetal bovine serum (FBS), 100 U ml^{-1} penicillin and 100 µg ml^{-1} streptomycin. When HEPG2 cells were compared directly to ECs in short term stable isotope tracing experiments, they were incubated in exactly the same medium as the ECs to rule out possible bias coming from the difference in media formulation. We did not perform authentication of the HEK293T and HEPG2 cells. *MOUSE LIVER ENDOTHELIAL CELLS (MLIECS)* were isolated from perfused healthy livers of control or GS^{ECKO} mice. Prior to perfusion, the mice were anesthetized with Nembutal (60 mg kg^{-1}). Mice were perfused with 5 ml of a water-based perfusion buffer containing 1.7 M NaCl, 84 mM KCl, 120 mM HEPES and 1 mM NaOH followed by 5 ml of a PBS-based digestion

644 buffer containing 0.1% collagenase II (Life Technologies), collagenase I (Life
645 Technologies), 2 mM $CaCl_2$, 1% antibiotic-antimycotic (Life Technologies) and 10% FBS
646 (Biochrome, Berlin, Germany) at a perfusion rate of 1 ml min^{-1}. Perfusion was considered
647 complete when the liver and mesenteric vessels were blanched and the desired amount of
648 digestion buffer (≥ 5ml) had passed through the circulatory system. Livers were dissected,
649 placed into a 50 ml conical tube with 3 ml of digestion buffer and incubated at 37 °C for
650 approximately 30 min, with regular shaking of the tubes every 5 min. After digestion, the
651 tissue was homogeneously dissociated and the reaction was stopped with 10 ml of
652 isolation buffer containing PBS + 0.1% BSA (Sigma-Aldrich). Subsequently, the cell
653 suspension was filtered through a 100 µm cell strainer and cells were washed twice with
654 isolation buffer. Finally, the ECs were isolated by magnetic bead sorting with Dynabeads
655 (CELLection™ Biotin Binder Kit, Life Technologies, Ghent, Belgium) coated with anti-
656 mouse CD31 (eBioscience, Anti-Mouse CD31 Clone 390), according to the manufacturer's
657 instructions. Briefly, the cell suspension was incubated with the beads at room
658 temperature for 30 min in HulaMixer® Sample Mixer (Life Technologies, Ghent, Belgium).
659 Next, $CD31^+$ ECs were collected by putting the tubes on a DynaMag™-50 Magnet (Life
660 Technologies) and removing the supernatant. The procedure was repeated twice to
661 remove cells debris. Finally, cells were resuspended in EGM2 medium (PromoCell) and
662 plated at the desired density on cell culture plates pre-coated with 0.1% gelatin, and grown
663 to confluency. *MOUSE ASTROCYTES* were prepared as described previously with minor
664 changes [27]. Briefly, spinal cords were dissected from 13-day old C57BL/6J mouse
665 embryos. Meninges and dorsal root ganglia were removed and a single cell population
666 was obtained by digestion with 0.05% trypsin in combination with gentle trituration. The
667 cell suspension was layered on a 6.2% OptiPrep™ (Axis-Shield, Oslo, Norway) cushion
668 and centrifuged at 500g for 15 min. The pellet was resuspended and the cells were plated
669 (12,000 cells cm^{-2}) in L15 medium supplemented with glucose (3.6 mg ml^{-1}), sodium

bicarbonate (0.2%), penicillin (100 IU ml^{-1}), streptomycin (100 μg ml^{-1}) and fetal bovine serum (10%). After reaching confluency, cell division was halted by treatment with cytosine arabinoside (10 μM, 3 days). After 4 weeks, more than 95% of cells stained positive for glial fibrillary acidic protein (GFAP; not shown). We routinely tested primary cells and cell lines for mycoplasma contamination with the MycoAlert mycoplasma detection kit (Lonza, LT07-418).

PLASMID CONSTRUCTIONS AND LENTIVIRAL PARTICLE PRODUCTION: cDNA for human *GS* was obtained from Origene. Silent mutations were introduced to make the *GS* cDNA resistant to the *GS*-specific shRNA (see below, TRCN0000045628). Point-mutated constructs were generated with Stratagene's QuickChange site-directed mutagenesis kit following manufacturer's guidelines. The cDNA for *RHOJ-EGFP* (*GFP-TCL*) was a gift from Channing Der (Addgene plasmid # 23231) [23] and was used as a template to generate the N-terminal truncated ΔN20-RHOJ-EGFP, lacking the first 20 amino acids and FLAG-tagged RHOJ. Standard cloning techniques were used to fuse GS to the photoswitchable fluorescent protein mEOS (pRSETa-mEos2 was a gift from Loren Looger; Addgene plasmid # 20341)[28]. The BiFC vector allowing simultaneous expression of two separate cDNAs fused to EGFP subfragment 1 (N-terminal; containing amino acids 1 to 158) or subfragment 2 (C-terminal; containing amino acids from 159 onwards) respectively was a kind gift of Prof. Hideaki Mizuno (KU Leuven). GS was fused to the N-terminal subfragment of EGFP and RHOJ was fused to the C-terminal EGFP subfragment to generate GS-$EGFP^{1/2}$, RHOJ-$EGFP^{2/2}$. Lentiviral expression constructs were obtained by cloning the respective cDNAs into pRRLsinPPT.CMV.MCS MM WPRE-vector. Validated *GS*-specific (TRC clones TRCN0000045628 (used in the majority of the experiments and indicated as GS^{KD1} in Extended Data Fig. 2a) and TRCN0000045631 (indicated as GS^{KD2} in Extended Data Fig. 2a and only used to confirm the migration and lamellipodial defect in Extended Data Fig. 3a-b) and *RHOJ*-specific (TRCN0000047606) shRNAs were either

used in the pLKO.1 vector or subcloned into the pLVX-shRNA2 vector (No. PT4052-5; Clontech, Westburg BV, Leusden, the Netherlands). Scrambled shRNAs or the empty vectors were used as negative controls (both with the same outcome). All constructs were sequence verified. Lentiviral particles were produced in HEK293T cells as previously described [2].

RECOMBINANT PROTEIN PRODUCTION: Template vectors pRRLhGS, pRRLhGS^{R324C} and pRRLhGS^{R341C} containing the gene encoding wild type or point mutated human *GS* were used as templates for PCR-based cloning. Recombinant constructs were expressed in the *Escherichia coli* strain BL21 codon + pICA2 that was transformed with pLH36-hGS in which expression is induced by isopropyl b-D-1-thiogalactopyranoside under control of a pL-promotor developed by the Protein Core of VIB (WO 98/48025, WO 04/074488). The pLH36 plasmid is provided with a His_6-tag followed by a murine caspase-3 site. The murine caspase-3 site can be used for the removal of the His_6-tag attached at the N-terminus of the protein of interest during purification. The transformed bacteria were grown in 200 ml Luria Bertani medium supplemented with ampicillin (100 µg ml^{-1}) and kanamycin (50 µg ml^{-1}) overnight at 28 °C before 1/100 inoculation in a 20 l fermenter provided with Luria Bertani medium supplemented with ampicillin (100 µg ml^{-1}) and 1 % glycerol. The initial stirring and airflow was 200 rpm and 1.5 l min^{-1}, respectively. Further, this was automatically adapted to keep the pO_2 at 30 %. The temperature was kept at 28 °C. The cells were grown to an optical density of A_{600nm} = 1.0, transferred at 20 °C, and expression was induced by addition of 1 mM isopropyl b-D-1-thiogalactopyranoside overnight. Cells were then harvested and frozen at -20 °C. After thawing, the cells were resuspended at 3 ml g^{-1} in 50 mM Hepes pH 7.5, 500 mM NaCl, 20mM imidazole, 1 mM phenyl-methylsulfonyl fluoride, 10 % glycerol, 5 mM β-mercaptoethanol, 1 mg per 100 ml DNAseI (Roche) and 1 tablet per 100 ml Complete Protease Inhibitor (Roche). The cytoplasmic fraction was prepared by using the Emulsiflex followed by centrifugation. All steps were

conducted at 4 °C. The clear supernatant was applied to a 20 ml Ni-Sepharose 6 FF column (GE Healthcare), equilibrated with 50 mM Hepes pH7.5, 500 mM NaCl, 20mM imidazole, 10 % glycerol, 5 mM β-mercaptoethanol and 1 mM phenyl-methylsulfonyl fluoride. The column was eluted with 50 mM Hepes pH 7.5, 500 mM NaCl, 400 mM imidazole, 10 % glycerol, 5 mM β-mercaptoethanol and 1 mM phenyl-methylsulfonyl fluoride after an intermediate elution step with 50 mM imidazole in the same buffer. Finally, the elution fraction was injected on a HiLoad 26/60 Superdex prep grade with 20 mM Hepes pH 7.5, 300 mM NaCL, 10 % glycerol and 0.5 mM TCEP as running solution. The obtained elution fractions were analyzed by SDS-PAGE. Recombinant protein concentration was determined using the Micro-BCA assay (Pierce).

***IN VITRO* KNOCK-DOWN/OVEREXPRESSION STRATEGIES:** To minimize off-target effects and other silencing artifacts, key findings were confirmed with at least two independent and validated *GS*-specific shRNAs (see above) and appropriate controls or with a *GS*-specific siRNA duplex (5'-GGAAUAGCAUGUCACUAAAGCAGGC-3') and scrambled control (TriFECTa^{TM}, IDT). For lentiviral transduction of shRNAs or overexpressing constructs an MOI of 10 or 5 was used, respectively. In case of simultaneous transduction of 2 different shRNAs, a MOI 7.5 was used for each individual shRNA. In case of simultaneous transduction of a shRNA in combination with an overexpression construct, the shRNA was transduced at MOI 10 and the overexpression construct at MOI 5, except for overexpression constructs for shRNA-resistant *GS* which were transduced at MOI 2.5. Transductions were performed on day 0 in the evening, cells were refed with fresh medium on day 1 in the morning and experiments were performed from day 3 or 4 onwards. siRNA transfection mixtures (in a total volume of 500 μl) were prepared in Opti-MEM containing GlutaMAX-I (Invitrogen) with Lipofectamine RNAi Max transfection reagent (Invitrogen, Belgium) according to the manufacturer's instructions. The mixtures were added to the cells (150,000 cells in 6 well-format plate) together with 2 ml EBM2 without antibiotics for

overnight transfection after which the medium was changed back to the regular M199 culture medium. siRNA transfection was done at least 48 h prior to functional assays. BiFC plasmids were transfected into HEK293T cells with Fugene® HD transfection reagent following the manufacturer's guidelines. KD efficiency and overexpression levels were closely monitored for each experiment either on mRNA (QRT-PCR) or protein level.

RNA ISOLATION AND GENE EXPRESSION ANALYSIS: Total RNA was extracted with Invitrogen's PureLink RNA mini kit according to the manufacturer's instructions; quality and quantity were measured on a Nanodrop (Thermo Scientific). cDNA synthesis was performed with the iScript cDNA synthesis kit (BioRad). Quantitative RT-PCR analyses were performed as previously described [1] on an Applied Biosystems 7500 Fast device with in house-designed primers and probes or premade primer sets (Applied Biosystems or Integrated DNA Technologies) for which sequences and/or primer set ID numbers are available upon request. *ENOX2* or *HPRT* were used as housekeeping genes.

WESTERN BLOTTING AND (CO-)IMMUNOPRECIPITATION: Proteins were extracted in Laemmli buffer (125 mM Tris-HCl (pH 6.8), 2% SDS,10% glycerol) or in RIPA buffer (25 mM Tris-HCl (pH 7.6), 150 mM NaCl, 1% NP-40, 1% sodium deoxycholate, 0.1% SDS) containing protease and phosphatase inhibitor mixes (Roche Applied Science). After shearing of genomic DNA, proteins in the lysates were separated by SDS-PAGE, transferred to nitrocellulose or polyvinylidene difluoride membranes and detected with specific antibodies and HRP-conjugated secondary antibodies in combination with ECL or SuperSignal Femto Western blotting substrate (Thermo Scientific). Signal was acquired with Image Quant LAS 4000 V 1.2 and densitometric quantification was done with ImageJ. For MLC and pMLC immunoblotting, each sample was loaded on two separate gels. One gel was used to detect MLC and the second was used to detect pMLC. Both gels had their own loading control, namely α-tubulin. pMLC/MLC was quantified as follows: (pMLC/α-tubulin)/(MLC/α-

773 tubulin), abbreviated in the figure panel as (c)pMLC/(c)MLC with (c) meaning 'corrected for
774 corresponding loading control'. Membrane *versus* cytosolic protein fractions were purified
775 with the Plasma Membrane Protein Extraction Kit (101Bio) according to the manufacturer's
776 guidelines and using proprietary buffers. For co-immunoprecipitation (co-IP) of
777 endogenous or overexpressed proteins, ECs were lysed by rotating at 4 °C during at least
778 4 h in co-IP lysis buffer (20 mM Tris-HCl pH8, 137 mM NaCl, 10% glycerol, 1% nonidet
779 NP-40 and 2 mM EDTA). Equal amounts of protein were incubated overnight with specific
780 antibodies or matching isotype control IgGs at 4 °C. Subsequently, 20 µl of protein A/G-
781 Sepharose beads was added to the immune complexes for 4 h at 4 °C under gentle
782 rotation. The beads were pelleted, washed three times with ice-cold co-IP lysis buffer and
783 boiled for 5 min in reducing agent and loading buffer prior to SDS-PAGE. To determine the
784 impact of deleting RHOJ's first 20 N-terminal AAs on the interaction with GS, co-IPs were
785 done as above on ECs simultaneously overexpressing GS and RHOJ-EGFP or ΔN20-
786 RHOJ-EGFP. In some of the experiments the expression of the ΔN20-RHOJ-EGFP was
787 lower than the expression of RHOJ-EGFP. To correct for this possible bias, densitometric
788 quantification of all bands was performed in ImageJ and signals in the IP lanes were
789 normalized to the input signals. The amount of GS IP'ed was the same in the RHOJ-EGFP
790 and ΔN20-RHOJ-EGFP condition (data not shown).

791 **BIOCHEMICAL AND METABOLIC ASSAYS:** *BICINCHONINIC ACID (BCA) ASSAY* (Pierce) was used to
792 determine protein content with Gen5 1.11.5 (BioTek Instruments). *LDH RELEASE* as a
793 measure for cell survival was determined with the Cytotoxicity Detection Kit (Roche
794 Applied Science) with Gen5 1.11.5 (BioTek Instruments). *INTRACELLULAR REACTIVE OXYGEN*
795 *SPECIES (ROS) LEVELS* were determined by CM-H_2DCFDA dye (Invitrogen) labeling
796 following manufacturer's guidelines. *GLUTAMINE SYNTHETASE ACTIVITY* in living cells. The
797 enzyme activity in living cells was determined by pulse-labeling the cells for 30 min with 2
798 mM $^{15}NH_4Cl$ and subsequent determination of ^{15}N incorporation in intracellular glutamine

by gas chromatography - mass spectrometry GC-MS (see below). Similarly, GS activity was measured by pulse-labeling for 30 min with 0.5 mM [U-^{13}C]-glutamic acid and subsequent tracing of ^{13}C into glutamine by GC-MS. The 0.025 mM glutamine condition was added to this assay for the sole purpose of having a positive control – lowering external glutamine levels should increase GS activity – and are not in any way reflecting maximal GS activity. Background signals were determined by pre-incubating the cells with the GS inhibitor MSO. As an independent manner (not relying on labeling one of the immediate substrates (NH_4^+ or glutamate)) to determine GS activity, we performed steady state labeling of ECs with [U-^{13}C]-glucose (5.5 mM) and determined carbon contribution to α-ketoglutarate, glutamate and glutamine (for labeling scheme see Extended Data Fig. 5f). Prior to derivatization for GC-MS analysis, cells were washed with ice-cold 0.9% NaCl and extracted in ice cold 80/20 methanol/water. *GLUTAMINE UPTAKE ASSAY*: Dynamic [U-^{13}C]-glutamine uptake assays were performed as follows: 2.5 x 10^5 cells/well were seeded in 6 well plates and pulse-labeled for 0, 0.5,10, 20 and 30 min with the regular M199 culture medium containing 0.6 mM [U-^{13}C]-glutamine instead of the regular 0.6 mM unlabeled glutamine. The 0 min time point represents an absolute negative control for which extracts were made from ECs that were never treated with tracer-containing medium. For the 0.5 min time point, the labeled medium was put on the cells and immediately aspirated (all together taking 0.5 min). At all time points, cells were thoroughly washed twice with ice-cold 0.9% NaCl to ensure complete removal of tracer-containing medium. Cellular extracts were then made in ice-cold 80/20 methanol/water, prior to derivatization for GC-MS measurements. Alternatively, cells were incubated with 0.5 μCi ml^{-1} [U-^{14}C]-L-glutamine for 10 min after which they were washed at least three times with ice-cold PBS. The last PBS wash was collected and checked for residual radioactivity. Cells were then lysed with 200 μl 0.2 N NaOH and lysates were neutralized with 20 μl 1 N HCl and used for scintillation counting. *[^{3}H]-THYMIDINE INCORPORATION*: Proliferation was determined by labeling the cells

with 1 µCi ml^{-1} [^{3}H]-thymidine for 2 h, followed by fixation in 100% ethanol for 15 min, precipitation with 10% trichloroacetic acid and finally lysis in 0.1 N NaOH. Scintillation counting was used to assess the amount of [^{3}H]-thymidine incorporated into the DNA. *ENERGY CHARGE ASSESSMENT:* 1.5 x 10^6 cells were collected in 100 µl ice cold 0.4 M perchloric acid containing 0.5 mM EDTA. pH was adjusted with 100 µl of 2 M K_2CO_3. 100 µl of the mixture was subsequently injected onto an Agilent 1260 HPLC with a C18-Symmetry column (150 x 4.6 mm; 5 mm; Waters), thermostated at 22.5 °C. Flow rate was kept constant at 1 ml min^{-1}. A linear gradient using solvent A (50 mM NaH_2PO_4, 4 mM tetrabutylammonium, adjusted to pH 5.0 with H_2SO_4) and solvent B (50 mM NaH_2PO_4, 4 mM tetrabutylammonium, 30% CH_3CN, adjusted to pH 5.0 with H_2SO_4) was accomplished as follows: 95% A for 2 min, from 2 to 25 min linear increase to 100% B, from 25 to 27 min isocratic at 100% B, from 27 to 29 min linear gradient to 95% A and finally from 29 to 35 min at 95% A. ATP, ADP and AMP were detected at 259 nm. *SEAHORSE EXTRACELLULAR FLUX MEASUREMENTS*: ECs were seeded at 1.5 x 10^5 cells per well on Seahorse XF24 tissue culture plates (Seahorse Bioscience Europe). Oxygen consumption (OCR) measurements were performed at 6 min intervals (2 min mixing, 2 min recovery, 2 min measuring) in a Seahorse XF24 device (XF Reader 1.8.1.1 software). Consecutive treatments with oligomycin (1.2 µM final), FCCP (5 µM final) and antimycin A (1 µM final) were performed to allow quantification of ATP-coupled OCR (OCR_{ATP}) and maximal respiration, next to basal OCR (OCR_{bas}). *GLYCOLYTIC FLUX:* ECs were cultured for 6 h in medium containing 0.4 mCi ml^{-1} [5-^{3}H]-D-glucose (Perkin Elmer) after which supernatant was transferred into glass vials sealed with rubber stoppers. ^3H_2O was captured in hanging wells containing a Whatman paper soaked with H_2O over a period of 48 h at 37 °C to reach saturation [1]. Then the paper was used for liquid scintillation counting (QuantaSmart TM V4 PerkinElmer). *^{14}C-GLUCOSE OXIDATION*: ECs were incubated for 6 h in medium containing 0.55 mCi ml^{-1} [6-^{14}C]-D-glucose. After that, 250 µl of 2 M perchloric

acid was added to each well to stop cellular metabolism and to release $^{14}CO_2$, which was captured overnight at room temperature in 1x hyamine hydroxide-saturated Whatman paper. The radioactivity in the paper was determined by liquid scintillation counting (QuantaSmart TM V4 PerkinElmer) [1]. *^{14}C-GLUTAMINE OXIDATION*: ECs were incubated for 6 h with medium containing 0.5 mCi ml^{-1} [U-^{14}C]-glutamine. 250 ml of 2 M perchloric acid was added to the cells to stop cellular metabolism and release $^{14}CO_2$. Trapping of $^{14}CO_2$ occurred as described above for glucose oxidation [1].

PROTEIN (AUTO)PALMITOYLATION DETECTION: *IN VITRO PALMITOYLATION (CLICK REACTION-BASED)*: Purified bacterial GS protein was incubated with the indicated concentration of palmitoyl alkyne-coenzyme A (Cayman Chemical) for 6 h at room temperature. The GS protein was then denatured by the addition of SDS. A click reaction with azide-biotin was performed to label the palmitoylated proteins [25]. Palmitoylated proteins were detected by SDS-PAGE followed by blotting with streptavidin-horseradish peroxidase. *FLUORESCENCE-BASED COA RELEASE DETECTION*: During autopalmitoylation of proteins, palmitate is transferred from palmitoyl-CoA to the protein thereby releasing reduced CoA. α-Ketoglutarate dehydrogenase can use CoA to convert α-ketoglutarate to succinyl-CoA, a reaction that features reduction of NAD^+ to fluorescent NADH[29]. In brief, recombinant human GS was incubated with palmitoyl-CoA in MES buffer at physiological pH for at least 1 h at 30 °C. The volume was then adjusted to 200 µl in 50 mM sodium phosphate buffer (pH 6.8) containing 2 mM α-ketoglutaric acid, 0.25 mM NAD^+, 0.2 mM thiamine pyrophosphate, 1 mM EDTA, 1 mM DTT and 32 mU α-ketoglutarate dehydrogenase. NADH levels were measured at 20 min after initiation of the reaction on a VICTOR plate reader (340 nm excitation – 465 nm emission). The experiment was performed in two directions: either with varying doses of palmitoyl-CoA for a fixed amount of recombinant GS or with varying amounts of recombinant GS for a fixed concentration of palmitoyl-CoA (40 µM). *AFFINITY CHROMATOGRAPHY*: A previously published protocol was used to

877 determine cell-free binding of recombinant human GS to palmitoyl-CoA agarose[30]. A total
878 of 50 µl of immobilized palmitoyl-CoA-agarose was equilibrated with 20 mM Tris-HCl (pH
879 8.4)/120 mM NaCl. The beads were incubated with 40 µg of recombinant human GS in a
880 final volume of 200 µl for 2 h at room temperature on a rotatory system. Beads were
881 pelleted and 20 µl of the supernatant was collected as the flow through (FT) fraction.
882 Beads were then washed eight times with 500 µl of 20 mM Tris-HCl (pH 8.4)/120 mM NaCl
883 buffer. 20 µl of the last wash fraction was collected as fraction W8. Beads were then eluted
884 with SDS loading buffer and heated for 15 min at 60 °C. 2 µg of recombinant protein was
885 used as input fraction (IF). IF, FT, W8 and SDS-eluate were analysed by immunoblotting
886 for GS. *IN CELL LABELING*: In cell labeling experiments were performed essentially as
887 described previously [25]. HEK-293T cells were transfected with the indicated expression
888 plasmids. Twenty-four h after transfection, the medium was replaced with DMEM + 10%
889 dialyzed FBS containing the indicated probes (50 µM 16C-YA or 50 µM 16C-BYA). After
890 18 h, cell lysates were collected by incubation of the cells on ice for 15 min in lysis buffer
891 (50 mM TEA-HCl (pH=7.4), 150 mM NaCl, 1% Triton X-100, 0.5% sodium deoxycholate,
892 0.1% SDS and 5 mM PMSF) followed by centrifugation for 10 min at 15,000 *g*. Equal
893 amounts of protein were then used for a click reaction with azide-biotin. For labeling with
894 17-ODYA, FLAG-RHOJ overexpressing ECs were incubated overnight with 17-ODYA (50
895 µM) in M199 supplemented with 3.6% fatty acid free BSA, 10% dialyzed FBS and 5 mM
896 sodium pyruvate. Cells were washed with ice-cold PBS and lysed in NaP lysis buffer (0.2
897 M $Na_2HPO_4.2H_2O$, 0.2 M $NaH_2PO_4.2H_20$, 1 M NaCl, 10% NP40). 2 µg of anti-Flag
898 antibody was conjugated to 20 µl of dynabeads protein G (Thermofisher) for 1 h at RT.
899 After washing the beads twice with NaP lysis buffer, at least 500 µg of protein was added
900 to the beads for 3 h at 4 °C. Then beads were washed 3 times with NaP lysis buffer and
901 resuspended in 20 µl of resuspension buffer (4% SDS, 50 mM TEA, 150 mM NaCl). The
902 click reaction was initiated by adding 0.5 µl of 5 mM tetramethylrhodamine azide (TAMRA)

(Lumiprobe), 0.5 µl 50 mM tris(2-carboxyethyl)phosphine hydrochloride (TCEP-HCl), 0.5 µl 10 mM tris[(1-benzyl-1*H*-1,2,3-triazol-4-yl)methyl]amine (TBTA) and 2.4 µl of 5 mM freshly made ascorbic acid. Samples were then incubated for 1 h at 37 °C in the dark. Sample buffer (9.4 µl) and reducing agent (3.7 µl) were added to stop the reaction. After 10 min at room temperature in the dark, samples were frozen at -80 °C or run on a 10% Bis-TRIS gel in MES buffer. In-gel fluorescence was imaged with Typhoon TM FLA 9500 V1.0. *STREPTAVIDIN-PULLDOWN*: After click reaction with azide-biotin, free azide-biotin was removed from the samples by centrifugal filtration column (Millipore). The samples were then incubated with streptavidin-conjugated beads for 1 h at room temperature. After washing with PBS-T, proteins were eluted from the beads by incubation in elution buffer (95% formamide, 10 mM EDTA (pH=8.0)) at 95 °C for 5 min. *ACYL-RESIN-ASSISTED CAPTURE (ACYL-RAC)* in which free cysteine thiols are chemically blocked and palmitoylated cysteines are exposed and captured by a resin, was performed with the CAPTUREome™ S-Palmitoylated Protein Kit (Badrilla) with minor adaptations to the manufacturer's guidelines. 500 µg of protein were incubated for 4 h in 500 µl of thiol blocking reagent (to block free thiols). Proteins were precipitated with ice-cold acetone and afterwards solubilized with 300 µl of binding buffer and spun down. After protein quantification, 30 µg was kept as total input fraction (IF), and equal amounts of protein were incubated for 2.5 h with (or without to obtain the negative control preserved bound fraction (pBF)) a thioester linkage specific cleavage reagent to cleave the thioester bond. Newly liberated thiols were captured with CAPTUREome™ resin. The resin was spun down and the supernate was collected as the cleaved unbound fraction (cUF) to check if the proteins of interest were indeed completely depleted from the thioester cleavage reagent (meaning efficient capture of the free thiols by the resin). After thorough washing of the resin, captured proteins (cleaved bound fraction (cBF)), were eluted with reductant and analyzed together with the IF, cUF and pBF by SDS-PAGE followed by immunoblotting.

GC-MS ANALYSIS: Metabolites from cells were extracted in 800 µl 80% methanol (at -80 °C). Next the extracts were centrifuged at 4 °C for 15 min at 20,000 x g and the supernatants were dried in a vacuum centrifuge. 25 µl of a 2% methoxyamine hydrochloride solution (20 mg dissolved in 1 ml pyridine) was added to the dried fractions which were then incubated at 37 °C for 90 min. Then 75 µl of N-tert-butyldimethylsilyl-N-methyltrifluoroacetamide with 1% N-tert-butyldimethyl-chlorosilane (Sigma-Aldrich) was added and the reaction was carried out for 30 min at 60 °C. Reaction mixtures were centrifuged for 15 min at 20,000 x g at 4 °C in order to remove insolubilities and the supernatant was transferred to a glass vial with conical insert (Agilent). GC-MS analyses were performed on an Agilent 7890A GC equipped with a HP-5 ms 5% Phenyl Methyl Silox (30 m - 0.25 mm i.d. - 0.25 µm; Agilent Technologies) capillary column, interfaced with a triple quadrupole tandem mass spectrometer (Agilent 7000B, Agilent Technologies) operating under ionization by electron impact at 70 eV. The injection port, interface and ion source temperatures were kept at 230 °C. Temperature of the quadrupoles was kept at 150 °C. The injection volume was 1 µl, and samples were injected at 1:10 split ratio. Helium flow was kept constant at 1 ml min^{-1}. The temperature of the column started at 100 °C for 5 min and increased to 260 °C at 2 °C min^{-1}. Next, a 40 °C min^{-1} gradient was carried out until the temperature reached 300 °C. After the gradient, the column was heated for another 3 min at 325 °C. The GC-MS analyses were performed in Single Ion Monitoring (SIM) scanning for the isotopic pattern of metabolites.

LC-MS ANALYSIS: *POLAR METABOLITES* were extracted using 250 µl of a 50-30-20 (methanol-acetonitrile-10 mM ammonium acetate pH 9.3 containing 2 µM of deuterated (d27) myristic acid as internal standard) extraction buffer. Following extraction, precipitated proteins and insolubilities were removed by centrifugation at 20,000 x g for 20 min at 4 °C. The supernatant was transferred to the appropriate mass spectrometer vials.

Measurements were performed using a Dionex UltiMate 3000 LC System (Thermo Scientific) in-line connected to a Q-Exactive Orbitrap mass spectrometer (Thermo Scientific). 15 μl of sample was injected and loaded onto a Hilicon iHILIC-Fusion(P) column (Achrom). A linear gradient was carried out starting with 90% solvent A (LC-MS grade acetonitrile) and 10% solvent B (10 mM ammonium acetate pH 9.3). From 2 to 20 mins the gradient changed to 80% B and was kept at 80% until 23 min. Next a decrease to 40% B was carried out to 25 min, further decreasing to 10% B at 27 min. Finally, 10% B was maintained until 35 min. The solvent was used at a flow rate of 200 μl min^{-1}, the column's temperature was kept constant at 25 °C. The mass spectrometer operated in negative ion mode, settings of the HESI probe were as follows: sheath gas flow rate at 35, auxiliary gas flow rate at 10 (at a temperature of 260 °C). Spray voltage was set at 4.8 kV, temperature of the capillary at 300 °C and S-lens RF level at 50. A full scan (resolution of 140,000 and scan range of m/z 70-1050) was applied. For the data analysis, we used an in-house library and metabolites of interest were quantified (area under the curve) using the XCalibur 4.0 (Thermo Scientific) software platform.

IN VITRO ASSAYS: *ENDOTHELIAL SPHEROID CAPILLARY SPROUTING* was performed following established protocols [1,2]. To form the spheroids, ECs were cultured overnight in hanging drops in EGM2 medium with methylcellulose (Sigma-Aldrich; 20 %volume of a 1.2% solution of methylcellulose 4000 cP). Spheroid sprouting entails both EC proliferation and migration. To have a 'clean' view on the migration aspect in sprouting, we also included conditions in which we blocked EC proliferation prior to sprout formation. More in particular, mitotic inactivation was achieved by adding mitomycin C (1 μg ml^{-1}) to the medium. To induce sprouting, spheroids were embedded in a collagen gel and incubated for 20 h. If required, chemical compounds (Fasudil at 10 μM, H1152 at 1 μM and Y26732 at 10 μM) were added during the collagen gel incubation step. Spheroids were then fixed with 4% paraformaldehyde and imaged under phase contrast illumination with a Motic AE

31 microscope (Motic Electric Group Co Ltd) or a Leica DMI6000B microscope (Leica Microsystems). Phase contrast images were used to quantify the number of sprouts per spheroid and the total sprout length (cumulative length of all sprouts on a spheroid). Spheroid body circumference was measured to correct for differences in size of the spheroid. Per experiment (*ie* per individual HUVEC isolation) at least 10 spheroids per condition were analyzed. *SCRATCH WOUND ASSAYS*: 75,000 HUVECs were seeded in 24-well format and were allowed to reach confluency over the next 24 h. At time T0 the confluent monolayer was scratched with a 200 μl pipet tip and photographed. The cells were further incubated for the indicated times and photographed again at time point Tx. Gap area at T0 minus gap area at Tx was measured with ImageJ and expressed as % migration distance. Per well, three non-overlapping regions along the scratch were analyzed. Much like the spheroid sprouting, scratch wound healing is a combined readout for EC migration and proliferation. Therefore, we also included conditions in which the ECs were pre-treated with mitomycin C (1 $\mu g\ ml^{-1}$) to rule out the effect of proliferation. *BOYDEN CHAMBER ASSAYS*: 50,000 HUVECs were seeded on 0.1% gelatin-coated transwells and allowed to adhere. Then, the transwells were washed and refed with medium containing only 0.1% FBS and placed in bottom wells containing medium with 5% FBS as a pro-migratory stimulus. 16 h later, transwells were processed and analysed for numbers of migrated cells. Pre-treatment with mitomycin C (see above) was applied. *VELOCITY OF RANDOM MOVEMENT* was assessed on HUVECs that were sparsely seeded on glass bottom 24-well plates. Time-lapse videos were generated by confocal image acquisition at 4 min intervals. Velocity of movement was determined by tracking nucleus position in function of time ($\mu m\ h^{-1}$) (Tracking Tool TM, Gradientech AB, Uppsala, Sweden). Per condition, on average 2 or 3 individual cells were traced in each biological repeat. *LAMELLIPODIAL AREA* was measured on sparsely seeded phalloidin-stained ECs with Leica MM AF morphometric analysis software (Leica Microsystems, Mannheim, Germany) with in-house

developed journals and is expressed in percent of total cell area. Treatment with MSO (1 mM), Y27632 (10 μM), Fasudil (10 μM), H1152 (1 μM), ML7 (15 μM) and peptide 18 (15 μM) were done 24 h prior to analysis of the cells. Per experimental condition, a minimum of ten individual cells was analyzed. *STAINING AND QUANTIFICATION OF VE-CADHERIN JUNCTIONS:* VE-cadherin staining and quantification of junctional length and gap index was performed as previously described [31]. First, the total junctional length (100%) was determined by summing up all segments, then the sum of all continuous segments was calculated as the percentage of total junctional length. The percentage difference between total and continuous represents the discontinuous length. Gap size index (intercellular gap area/cell number) was determined with the formula ([intercellular gap area/total cell area] ×1,000)/cell number. Junctional lengths, intercellular gap area, and total cell area were defined manually with ImageJ. For each condition, a minimum of 10 fields was quantified (10-15 cells per field on average) per experiment, and data shown represent the mean of at least 3 independent experiments. *TRANS ENDOTHELIAL ELECTRICAL RESISTANCE (TEER):* 50,000 ECs were seeded on 6.5 mm 0.1% gelatin-coated polyester transwells, 0.4 μm pore size (Costar ref. 3470, Sigma-Aldrich). The electrical resistance was measured with an Endhome-6 electrode (World Precisions Instruments) connected to an EVOM2 voltohmmeter (World Precisions Instruments). Gelatin-coated wells without cells were used to measure the intrinsic electrical resistance of the inserts for background subtraction. Measurements were performed every day for 4 consecutive days, with at least 2 measurements per condition.

ACTIN DYNAMICS AND RHO (KINASE) ACTIVITY ASSAYS: *LATRUNCULIN WASH-OUT*: ECs were treated with latrunculin B (100 ng ml^{-1}) for 30 min and were then washed three times with culture medium. The cells were fixed at the indicated time points and stained with phalloidin to visualize actin stress fibers. *THE F-/G-ACTIN RATIO* in GS^{KD} *vs* control ECs was determined in 4% paraformaldehyde-fixed cells which were permeabilized for 10 min in

PBS with 0.2% Triton X-100 and stained with phalloidin-Alexa 488 and deoxyribonuclease I-Alexa 594 (1:200) [32]. Fluorescence intensities were quantified with ImageJ and were based on gray values. On average, ten individual cells were analyzed per experimental condition. For *RHOJ ACTIVITY* measurements, cells were lysed in buffer containing 50 mM Tris, pH 7.6, 150 mM NaCl, 1% Triton X-100, 0.5 mM $MgCl_2$, protease inhibitors and 0.1 $\mu g\ \mu l^{-1}$ biotinylated CRIB-peptide. After spinning down for 4 min at 14,000 rpm at 4 °C, 50 µl streptavidin-coated beads were added to the lysates. Subsequently, samples were rotated for 30 min at 4 °C, beads were washed 4 times in the above buffer after which they were boiled for 5 min in reducing agent and loading buffer [33]. As negative controls in this assay, we used lysates from $RHOJ^{KD}$ ECs, a streptavidin beads only-condition and lysates in which the biotinylated CRIB-peptide was replaced by an irrelevant biotinylated protein (Fig. 4c). *RHOA/B/C ACTIVITY* was determined with GST-Rhotekin pull down assays following previously established protocols [34]. *ROCK ACTIVITY* was assayed by determining phosphorylation of the ROCK target myosin light chain 2 (MLC2) on Western Blot or by immunostaining. Fluorescence intensities from immunostainings were quantified with ImageJ and were based on gray values.

CONFOCAL AND HIGH RESOLUTION IMAGING: *CONFOCAL IMAGING* was performed on a Zeiss LSM 510 Meta NLO or Zeiss LSM 780 confocal microscope (oil objectives: x 40 with NA 1.3, x 63 with NA 1.4, x 100 with NA 1.3) with ZEN 2011 software (Carl Zeiss, Munich, Germany). Within individual experiments, all images across different experimental conditions were acquired with the same settings. *DORA RHOA BIOSENSOR FRET IMAGING*: RHOA activity was measured in living HUVECs by monitoring yellow fluorescent protein (YFP) FRET over donor cyan fluorescent protein (CFP) intensities as described previously [35]. In brief, a Zeiss Observer Z1 microscope, with a Chroma 510 DCSP dichroic splitter, two Hamamatsu ORCA-R2 digital CCD cameras and an attached dual camera adaptor (Zeiss) controlling a 510 DCSP dichroic mirror, was used for simultaneous monitoring of

CFP and YFP emissions using filter sets ET 480/40 and ET 540/40m (Chroma Technology, Rockingham, USA), respectively. To excite the CFP donor, ET 436/20x and 455 DCLP dichroic mirror was used (Chroma). For FRET/CFP ratiometric processing, CFP and YFP images were processed using the MBF ImageJ collection. The images were background-subtracted, aligned and a threshold was applied. Finally, the FRET/CFP ratio was calculated and a custom lookup table was applied to generate a color-coded image, in which white and red colors illustrate high and blue colors illustrate low RHOA activities. *BiFC IMAGING AND QUANTIFICATION*: BiFC was evaluated using a laser scanning microscope (Fluoview FV1000, Olympus, Tokyo, Japan) equipped with a UPLSAPO 60x Oil objective (NA1.35). Before imaging cells were fixed with 4 % (v/v) paraformaldehyde and stained with DAPI (1:1,000 dilution, Invitrogen). A 488-nm laser was used for exciting EGFP while DAPI was excited using a 405-nm laser. A DM405/488/559/635 polychroic mirror was used to guide the excitation lasers to the sample. Fluorescence images of fixed cells were acquired using a sampling speed of 4 µs pixel^{-1}. Emission light was collected at 430-470 and 500-550 nm, for DAPI and EGFP, respectively. The images were acquired with a pixel size of 207 nm (1,024 x 1,024 pixels). BiFC was first established in HEK cells expressing GS-EGFP$^{1/2}$ and RHOJ-EGFP$^{2/2}$ from one expression vector, with a construct overexpressing an unfused N-terminal EGFP half-site together with RHOJ coupled to the C-terminal EGFP half-site as a negative control (data not shown). To determine the effect of deleting the first 20 amino acids in RHOJ on BiFC in ECs, separate expression constructs for GS-EGFP$^{1/2}$, RHOJ-EGFP$^{2/2}$ and ΔN-RHOJ-EGFP$^{2/2}$ were used (Ext. Data Fig. 7e). Quantification of expression efficiency was done using a home-built routine in Matlab®. *TIRF MICROSCOPY*: A home build setup based on an inverted microscope (IX83, Olympus) was used to detect single molecules under total internal reflection (TIRF) mode. The setup was equipped with an Electron Multiplying-CCD cameras (ImagEM C9100-13; Hamamatsu Photonics, Hamamatsu, Japan) and an APON 60XOTIRF objective lens (NA

1.49, Olympus). The GS-mEos3.2 molecules were excited with a 561-nm line from a DPSS laser (200 mW; Coherent Inc., Santa Clara, California) and converted with a 405-nm line from a diode laser (Cube, 100 mW; Coherent Inc., Santa Clara, California). Before being expanded, the laser lines were combined using a 405bcm dichroic mirror. The laser lines were guided onto the sample by a dichroic mirror, z488/561/633rpc. The fluorescence of the red of mEos3.2 form was detected through a long pass filter 572 (HQ572LP), in combination with a band pass filter HQ590M40-2P. All the filters were purchased from Chroma Inc. Time-lapse fluorescence images were recorded with continuous illumination at a 62.5 Hz acquisition rate (16 ms per frame). *SINGLE PARTICLE TRACKING (SPT)*: For calculation of single molecule coordinates the program 'Localizer' running from Matlab was used [36]. After localization, the positions of a molecule detected in consecutive frames are connected to reconstruct a trajectory using home-developed software in Matlab. Coordinates presented in consecutive frames are linked to form a single trajectory when they uniquely appear in a distance smaller than 856 nm (corresponding to 8 pixels). Trajectories with at least 3 steps were analyzed using variational Bayes single particle tracking analysis (vbSPT), a software package for analysis of single particle diffusion trajectories, where the diffusion constants switch randomly according to a Markov process [37].

MICE: *GS^{ECKO} MICE*: To obtain inducible EC-specific GS knock-out mice, *$GS^{lox/lox}$* mice [38] were intercrossed with *VECadherin-Cre^{ERT2}* [39] or with *Pdgfb-Cre^{ERT2}* [40] mice and named GS^{vECKO} and GS^{pECKO} respectively. Correct Cre-mediated excision of the loxed *GS* segment in tamoxifen-treated GS^{ECKO} mice was confirmed via PCR analysis of genomic DNA (Extended Data Fig. 1d-e). *GENERATION OF $GS^{+/GFP}$ CHIMERAS* : Blastocysts were collected from superovulated C57BL/6 females at post-coital day 3.5 and were cultured for 5-8 days in ES cell culture medium consisting of Knockout DMEM medium (Invitrogen), with 2 mM L-glutamine, fetal bovine serum (Hyclone, ThermoScientific), MEM non-

essential amino acids 100X (Invitrogen), 0.01 mM β-mercaptoethanol (Sigma-Aldrich), 1 mM sodium pyruvate (Invitrogen), 100 U ml^{-1} penicillin, 100 μg ml^{-1} streptomycin, and 2,000 U ml^{-1} Leukemia Inhibitory Factor (Merck, Millipore). Afterwards, the inner cell mass was selectively removed from the trophectoderm, trypsinized and replated on a Mitomycin C-arrested MEF feeder monolayer. ES cells were fed every day and passaged every 2-4 days onto new feeder cells. *$GS^{+/GFP}$* ES cells (E14IB10 ES cell line) [6] were injected into C57BL/6 blastocysts and high chimeric pups were killed at P5 for detection of GFP in the retinal microvasculature.

***IN VIVO* MODELS:** *ANALYSIS OF DORSAL DERMAL BLOOD VESSEL NETWORK*: From E11.5 to E13.5 after vaginal plug, GS^{vECKO} pregnant dams were treated with tamoxifen (50 mg kg^{-1}) by oral gavage. At E16.5 they were euthanized by cervical dislocation after which embryos were dissected from the uterus. Yolk sacs were collected, washed with PBS and used for genotyping of the embryos. The embryos were fixed for 10 min in 1% PFA prior to dissection of the dorsal skin. The epidermal and dermal layers were separated under a dissection microscope. Dissected back skins were permeabilized overnight (0.5% Triton X-100, 0.01% sodium deoxycholate, 1% bovine serum albumin, 0.02% sodium azide) prior to whole-mount immunostaining with CD31. To systematically analyze the same region for each embryo, 1 rectangular confocal image (1,700 x 1,100 μm) was taken at the anterior side of the skin specimen with the upper longer side of the rectangle placed on the midline. Within each rectangular picture the number of branch points was determined with the cell counter tool in ImageJ in 6 ROIs (250 x 250 μm), 3 in the top half and 3 in the bottom half of the rectangle, not overlapping with the larger arteries and veins. *NEONATAL RETINAL ANGIOGENESIS*: EC-specific GS deletion was obtained by IP administration of tamoxifen (Sigma; 10 mg kg^{-1}; dissolved in 1:10 EtOH:oil solution) once daily from P1 to P3 in GS^{vECKO} or once at P2 for GS^{pECKO}. For *in vivo* proliferation quantification, EdU (5-ethynyl-2´-deoxyuridine; Invitrogen) was injected IP 2 h before sacrifice. Unless stated

otherwise, retinas were isolated at P5 as previously described [41] and fixed in 2% PFA for 2 h. Isolectin B4 (IB4), EdU, NG2 and ColIV stainings were performed as previously described [1,2]. Radial outgrowth of the vascular plexus, vascular area, branch points, number of filopodia and number of distal sprouts were analysed on isolectin IB4-stained retinas (see below) with Image J. Numbers of branch points and EdU^+ ECs were quantified in 200 x 200 μm ROIs; per retina 12 ROIs were placed at the front of the vascular plexus and 8 ROIs were placed more towards the center of the plexus. Filopodia and distal sprouts were quantified on ten high magnification (63x) images per retina, each representing approximately 200 μm of utmost vascular front. For analysis of the retinal vasculature at P21 (3 week-old) and P42 (6 week-old) mice underwent the same tamoxifen treatment regimen as for analyses at P5. In addition, different tissues were collected from P42 mice for endoglin and CD34 staining to study blood vessels in different vascular beds. *OXYGEN INDUCED RETINOPATHY:* Oxygen induced retinopathy (ROP) was induced by exposing C57BL/6 pups to 70% oxygen from P7-P12. Pups were then returned to normoxia and injected daily with 20 mg kg^{-1} MSO. At P17, pups were euthanized and eyes were enucleated, fixed in 4% PFA and retinal flatmounts were stained for isolectin B4 [2,3]. MSO-treated animals retained normal behavior notwithstanding observable weight loss. Mosaic tile images were captured using the inverted Leica DMI6000B epifluorescence microscope (Leica, Manheim, Germany) and analysis of the vascular tuft area (the complete retina was analyzed, no ROIs were used) and the vaso-obliterated area was performed with NIH Image J software and are expressed as percentage of the total retinal area. *CORNEAL (MICRO-)POCKET ASSAY (CPA)* to induce neovascularization of the avascular cornea was performed as previously described [42]. In brief, in the eyes of 8 week-old C57BL/6 mice, a lamellar micropocket was dissected toward the temporal limbus to allow placing of a basic fibroblast growth factor (bFGF)-containing pellet on the corneal surface. Five days after implanting the pellets, the mice were sacrificed, the eyes were

enucleated and the corneas were excised and fixed in 70% ethanol prior to CD31 antibody staining. After staining, the corneas were flat-mounted and imaged on a Zeiss LSM 780 confocal microscope. $CD31^+$ area was measured in ImageJ after thresholding the signal and is expressed as % of total cornea area. Production of the pellets was done as previously described [42]. The pellets contained 20 ng bFGF and the concentration of MSO in the initial solution from which the pellets were made was 10 mM. *IMIQUIMOD-INDUCED SKIN INFLAMMATION:* Ten week old female Balb/C mice received a daily topical dose of 5% imiquimod cream (62.5 mg) on their shaved backs for four days to induce skin inflammation [3]. 1 h after each administration of the cream, the same skin area was treated either with Vaseline® jelly or Vaseline® jelly containing MSO (low dose: 20 mg kg^{-1}; or high dose: 40 mg kg^{-1}). The MSO treatment did not affect bodyweight of the mice. Skins and spleens were collected and fixed in 4% PFA. Paraffin sections of skins were stained for CD105 (R&D Systems) and H&E. Images were captured with a Leica DMI6000B microscope (Leica microsystems, Mannheim, Germany). Per animal, ten images representing different locations along the total length of the skin specimen were analyzed for $CD105^+$ area. *MILES VASCULAR PERMEABILITY ASSAY:* 8 week old female Balb/C mice were treated for 3 consecutive days with 20 mg kg^{-1} day^{-1} MSO or with vehicle prior to injection with 300 μl 0.5 % Evan's blue dye. The inflammatory irritant mustard oil (0.25 ml allyl isothiocyanate in 4.75 ml mineral oil) was applied on one of the ears with a cotton swab to induce vascular permeability. Mineral oil as a control was applied on the other ear. After 15 min, again mustard oil/mineral oil was applied on the ear for 30 min, after which the circulation was flushed with saline for 3 min and mice were perfused with 1 % PFA in 50 mM citrate buffer (pH=3.5) for 2 min. Ears were cut and minced in formamide and incubated at 55 °C overnight to extract the Evan's blue from the tissue. Quantification of the dye was performed by a spectrophotometrical optical density measurement at 620 nm. *HEMATOLOGICAL PROFILING IN 6 WEEK-OLD MICE* was performed with a Cell Dyn 3700 device

(Abbott Diagnostics) according to the manufacturer's guidelines. Plasma measurements for different liver/inflammation parameters were performed in the clinical laboratory of the university hospital of Leuven. Prior randomization was not applicable for any of the above mouse models given that all animal treatments were done in baseline conditions. No statistical methods were used to predetermine the sample size. For all mouse experiments, data analysis was done by researchers blinded to the group allocation. All animal procedures were approved by the Institutional Animal Care and Research Advisory Committee of the University of Leuven.

IN SILICO SCREENING FOR PALMITOYLATION SITES: The human RHOJ protein sequence was screened for putative palmitoylation sites on the SwissPalm website [22] entering 'RHOJ' as the protein name.

MODELING AND SIMULATIONS: The GS models were built starting from X-ray crystallographic structures retrieved from the Protein Data Bank (entry 2OJW for human GS and 1FPY for bacterial GS). All simulations were run with Gromacs 5.1.4[43] and the Amber FF14SB[44] force field, while palmitoyl-CoA was parametrized with GAFF and the point charges were calculated with Gaussian 09[45] at the Hartree-Fock level with a 6-31G* basis set. The different models were then embedded in a TIP3P water box, counter ions were added to ensure the overall charge neutrality. An initial 2,000 steps of steepest descent and 500 steps of conjugated gradient were applied to minimize the geometry and remove steric clashes, followed by 10 ns of isothermal-isobaric (NPT) equilibration. The Berendsen barostat was applied to keep the pressure around 1 atm, while the temperature of 300K was maintained throughout all the simulations with the V-rescale algorithm[46]. 500 ns long molecular dynamics production runs were carried out for all the systems in the canonical (NVT) ensemble, for a cumulative total of 2.5 μs. The particle mesh Ewald (PME)-Switch algorithm was used for electrostatic interactions with a cut-off of 1 nm, and a single cut-off

of 1.2 nm was used for Van der Waals interactions. Four simulations for human GS and two for *Salmonella typhimurium*'s GS were run by placing the CoA moiety close to the adenosine binding site and allowing different initial positions for the palmitoyl tail. The CoA head invariably docked and remained tightly bound to the adenine binding site in all simulations. Among these, two favorable alternative arrangements (Extended Data Fig. 8b) for the tail were identified in both systems. In one of these conformations, the beginning of the palmitate tail (from the point of view of the CoA moiety) approaches very closely the conserved CYS209 (human residue numbering, Conformation A in Extended Data Fig. 8b, details in Extended Data Fig. 8c), and in the other conformation (Conformation B in Extended Data Fig. 8b, details in Extended Data Fig. 8d) it approaches the conserved Ser65 and 75.

MULTIPLE SEQUENCE ALIGNMENTS: A multiple sequence alignment of the GS protein across different species was performed with the Basic Local Alignment Search Tool (BLAST). The algorithm matches sequences according to local similarity, by optimizing their Maximal Segment Pair score (MSP). The 100 matches with the highest identity to the *Homo sapiens* sequence surrounding amino acid C209 were taken from the UniProtKB/Swiss-Prot refined database.

STATISTICAL ANALYSIS: Data represent mean±s.e.m. of pooled experiments unless otherwise stated. Scatters in bar graphs represent the values of independent experiments or individual mice. In case individual values are highly alike, scatter points overlap and may no longer be visible as individual points. n values represent the number of independent experiments performed or the number of individual mice phenotyped. Statistical significance between groups was calculated with one of the following methods. For comparisons to point-normalized data, a two-tailed one-sample *t*-test was used in GraphPad Prism7. For pairwise comparisons, two-tailed unpaired *t*-tests were used in

GraphPad Prism7. For multiple comparisons within one data set, one-way ANOVA with Dunnett's multiple comparison (comparing every mean with the control mean rather than comparing every mean with every other mean) was used in GraphPad Prism7. Mixed model statistics (this test does not assume normality or equal variance) was used with the experiment as random factor only in case confounding variation in baseline measurements between individual EC isolations (for each experiment, ECs were freshly isolated from individual human umbilicals) or mouse litters precluded the use of the above described statistical tests. For this, R and the *lme4* package were used; *P* values were obtained with the Kenward-Roger F-test for small mixed effect model datasets. In the most severe cases, the individual datapoints (each datapoint being the mean of the technical replicates within an experiment or an individual animal) in the bar graphs have been color-coded per experiment or per litter to show the baseline variation. Sample size for each experiment was not pre-determined. A *P* value <0.05 was considered significant.

DATA AVAILABILITY: Fig.1, Fig. 4, Fig. 5, Extended Data Fig. 1, Extended Data Fig. 7 and Extended Data Fig. 8 have associated raw data (uncropped blots and/or gel pictures) in Supplemental Information Fig. 1. Fig. 1, Fig. 2, Extended Data Fig. 1 and Extended Data Fig. 4 have associated raw data (Excel files) for all bar graphs representing data from experiments involving mouse models. For the molecular modelling of palmitoyl-CoA docking into GS, models and trajectories are available on Figshare (doi: 10.6084/m9.figshare.6575438). Any additional information required to interpret, replicate or build upon the Methods or findings reported in the manuscript is available from the corresponding author upon request.

REFERENCES UNIQUE TO THE METHODS SECTION

25 Zheng, B., Zhu, S. & Wu, X. Clickable analogue of cerulenin as chemical probe to explore protein palmitoylation. *ACS Chem Biol* **10**, 115-121, doi:10.1021/cb500758s (2015).

26 Martin-Ramirez, J., Hofman, M., van den Biggelaar, M., Hebbel, R. P. & Voorberg, J. Establishment of outgrowth endothelial cells from peripheral blood. *Nat Protoc* **7**, 1709-1715, doi:10.1038/nprot.2012.093 (2012).

27 Van Den Bosch, L., Vandenberghe, W., Klaassen, H., Van Houtte, E. & Robberecht, W. Ca(2+)-permeable AMPA receptors and selective vulnerability of motor neurons. *J Neurol Sci* **180**, 29-34 (2000).

28 McKinney, S. A., Murphy, C. S., Hazelwood, K. L., Davidson, M. W. & Looger, L. L. A bright and photostable photoconvertible fluorescent protein. *Nat Methods* **6**, 131-133, doi:10.1038/nmeth.1296 (2009).

29 Hamel, L. D., Deschenes, R. J. & Mitchell, D. A. A fluorescence-based assay to monitor autopalmitoylation of zDHHC proteins applicable to high-throughput screening. *Anal Biochem* **460**, 1-8, doi:10.1016/j.ab.2014.05.013 (2014).

30 Kummel, D., Heinemann, U. & Veit, M. Unique self-palmitoylation activity of the transport protein particle component Bet3: a mechanism required for protein stability. *Proc Natl Acad Sci U S A* **103**, 12701-12706, doi:10.1073/pnas.0603513103 (2006).

31 Fraccaroli, A. *et al.* Endothelial alpha-parvin controls integrity of developing vasculature and is required for maintenance of cell-cell junctions. *Circulation research* **117**, 29-40, doi:10.1161/CIRCRESAHA.117.305818 (2015).

32 Ho, C. Y., Jaalouk, D. E., Vartiainen, M. K. & Lammerding, J. Lamin A/C and emerin regulate MKL1-SRF activity by modulating actin dynamics. *Nature* **497**, 507-511, doi:10.1038/nature12105 (2013).

33 Timmerman, I. *et al.* A local VE-cadherin and Trio-based signaling complex stabilizes endothelial junctions through Rac1. *J Cell Sci* **128**, 3041-3054, doi:10.1242/jcs.168674 (2015).

34 van Buul, J. D. *et al.* RhoG regulates endothelial apical cup assembly downstream from ICAM1 engagement and is involved in leukocyte trans-endothelial migration. *J Cell Biol* **178**, 1279-1293, doi:10.1083/jcb.200612053 (2007).

35 Heemskerk, N. *et al.* F-actin-rich contractile endothelial pores prevent vascular leakage during leukocyte diapedesis through local RhoA signalling. *Nat Commun* **7**, 10493, doi:10.1038/ncomms10493 (2016).

36 Dedecker, P., Duwe, S., Neely, R. K. & Zhang, J. Localizer: fast, accurate, open-source, and modular software package for superresolution microscopy. *J Biomed Opt* **17**, 126008, doi:10.1117/1.JBO.17.12.126008 (2012).

37 Persson, F., Linden, M., Unoson, C. & Elf, J. Extracting intracellular diffusive states and transition rates from single-molecule tracking data. *Nat Methods* **10**, 265-269, doi:10.1038/nmeth.2367 (2013).

38 He, Y. *et al.* Glutamine synthetase deficiency in murine astrocytes results in neonatal death. *Glia* **58**, 741-754, doi:10.1002/glia.20960 (2010).

39 Benedito, R. *et al.* The notch ligands Dll4 and Jagged1 have opposing effects on angiogenesis. *Cell* **137**, 1124-1135, doi:S0092-8674(09)00324-9 [pii] 10.1016/j.cell.2009.03.025 (2009).

40 Claxton, S. *et al.* Efficient, inducible Cre-recombinase activation in vascular endothelium. *Genesis* **46**, 74-80, doi:10.1002/dvg.20367 (2008).

41 Pitulescu, M. E., Schmidt, I., Benedito, R. & Adams, R. H. Inducible gene targeting in the neonatal vasculature and analysis of retinal angiogenesis in mice. *Nat Protoc* **5**, 1518-1534, doi:10.1038/nprot.2010.113 (2010).

42 Kenyon, B. M. *et al.* A model of angiogenesis in the mouse cornea. *Invest Ophthalmol Vis Sci* **37**, 1625-1632 (1996).

43 Abraham, M. J. *et al.* GROMACS: High performance molecular simulations through multi-level parallelism from laptops to supercomputers. *SoftwareX* **1**, 19-25 (2015).

44 Maier, J. A. *et al.* ff14SB: Improving the Accuracy of Protein Side Chain and Backbone Parameters from ff99SB. *J Chem Theory Comput* **11**, 3696-3713, doi:10.1021/acs.jctc.5b00255 (2015).

45 Frisch, M. *et al.* Gaussian 09, Revision C.01. Gaussian Inc., Wallingford CT. (2009).

46 Bussi, G., Donadio, D. & Parrinello, M. Canonical sampling through velocity rescaling. *J Chem Phys* **126**, doi:Artn 014101 10.1063/1.2408420 (2007).

LEGENDS TO EXTENDED DATA TABLES

EXTENDED DATA TABLE 1: WEIGHT, HEMATOLOGICAL AND BLOOD PLASMA PARAMETERS FOR 6 WEEK-OLD GS^{vECKO} MICE AND CONTROL LITTERMATES

Values are mean±s.e.m. of n=14 (control) *vs* n=17 (GS^{vECKO}) animals. **P* = 0.0232 *vs* control, Student's *t* test. WBCs, white blood cells; RBCs, red blood cells, AST, aspartate amino transferase; ALT, alanine amino transferase; γ-GT, gamma-glutamyl transferase; CRP; C-reactive protein.

EXTENDED DATA TABLE 2: ALIGNMENT OF THE AMINO ACID SEQUENCE ENCOMPASSING THE C209 RESIDUE ACROSS DIFFERENT SPECIES.

Multiple sequence alignment showing the conservation of amino acid C209 (in red) in GS across different species. Here the sequence alignment of 41 residues surrounding this cysteine is shown for up to 100 of the closest sequence identity matches with *Homo sapiens* GS obtained with BLAST from the UniProtKB/Swiss-Prot database. C209 is mostly conserved across species and when not conserved it is often substituted by residues (Ser or Thr) that can (in theory) be palmitoylated as well. In *Escherichia coli* (shown at the bottom), for example, a Thr is found at the structurally equivalent position (T210, highlighted in yellow). If for one and the same species multiple GS isoforms are known, only the one with the highest % identity is shown.

LEGENDS TO EXTENDED DATA FIGURES

EXTENDED DATA FIGURE 1: *GS* KNOCK-OUT IMPAIRS VESSEL SPROUTING

a, *GS* mRNA levels in human umbilical vein ECs (HUVEC; n=9 donors), lung ECs (n=5), colon ECs (n=4), liver ECs (n=3), human umbilical arterial ECs (HUAEC; n=2) and human blood outgrowth ECs (BOEC (n=2); (mean±s.e.m.; **P* <0.05 *vs* HUVEC, Student's *t* test) and in HEPG2 cells (mean±s.e.m.; n=3; **P* <0.05 *vs* HUVEC, Student's *t* test). **b-c,** Western blot of GS protein levels in HUVECs and HEPG2 cells in medium containing 0.6 mM glutamine (+) or 0.025 mM glutamine (-) (b), and in isolated mouse liver ECs (mLiECs)

and mouse astrocytes (c) (representative immunoblots of two independent experiments are shown). **d-e,** Genomic organization of the loxed *GS* allele before and after Cre-mediated excision (d) and correct recombination of the lox allele (L) in GS^{vECKO} and GS^{pECKO} mice upon tamoxifen (tam) treatment, as assessed by genomic DNA PCR (e; the PCR to amplify the loxed *GS* allele (lox) or to amplify the Cre-recombined allele (Δ) were run in separate reactions but loaded in the same lane; the gel picture shown is representative for all control, vECKO and pECKO mice used in this study). **f,** Quantification of branchpoints at the rear of the plexus in GS^{vECKO} mice (mean±s.e.m.; n=10 animals for GS^{vECKO} and 11 for wild-type (WT) controls from 3 litters; $^{*}P<0.05$ *vs* WT littermates, mixed models R statistics). **g,** Pericyte coverage of retinal microvessels in WT and GS^{vECKO} littermates determined by NG2 staining and shown as $NG2^{+}$ area as % of vessel area (mean±s.e.m.; n=4 animals for WT and 3 for GS^{vECKO} from 1 litter; $^{NS}P>0.05$ *vs* WT, Student's *t* test). **h,** Reduced complexity of the retinal vascular front in P5 GS^{vECKO} *vs* WT animals determined by the number of branches on distal sprouts (mean±s.e.m.; n=13 animals for WT and 21 for GS^{vECKO} from 5 litters; $^{*}P<0.05$ *vs* WT, Student's *t* test). **i,** Quantification of EdU^{+} ECs at the rear of the plexus (mean±s.e.m.; n=12 animals for WT and 22 for GS^{vECKO} from 4 litters; $^{NS}P>0.05$ *vs* WT littermates, Student's *t* test). **j-m,** Isolectin B4 staining of P5 retinal vascular plexi from WT (j) and GS^{pECKO} (k) mice (representative pictures with zoom-in insets, A=artery, V=vein) and quantification of branch points at the front (l) and the rear (m) of the plexus (mean±s.e.m.; n=10 animals for WT and 18 for GS^{pECKO} from 4 litters; $^{*}P\leq0.05$ *vs* WT littermates, Student's *t* test). **n-u,** Isolectin B4 staining of the retinal microvasculature of 3 week (P21)-old (n,o) and 6 week (P42)-old (r,s) WT and GS^{vECKO} littermates (A=artery, V=vein). Lower left insets display higher magnification of IB4-stained superficial plexus, whereas lower right insets display higher magnification of the deep plexus. Also shown is the corresponding quantification of the vascular area (p,t) and the branch point density (q,u) in the superficial and the deep

layer (mean±s.e.m.; n=8 animals for WT and 8 for GS^{vECKO} at P21, from two litters; n=10 animals for WT and 14 for GS^{vECKO} at P42, from four litters; $^{NS}P>0.05$ *vs* WT, Student's *t* test). **v-ag,** Representative micrographs of heart (v,z), liver (w,aa) and kidney (x,ab) sections from WT and GS^{vECKO} littermates immunostained for the EC marker endoglin and of lung (y,ac) sections immunostained for the EC marker CD34 and corresponding quantifications of endoglin$^+$ (ad, heart; ae, liver; af, kidney) or CD34$^+$ (ag) vascular area (mean±s.e.m.; n=5 animals (4 for heart) for WT and 7 (6 for heart) for GS^{vECKO}, from two litters, $^{NS}P>0.05$ *vs* WT, Student's *t* test). **ah-ai,** Images of flat-mounted retinas from control (ah) and MSO-treated (ai) ROP mice (vaso-obliterated area in white). Images shown are representative for 7 (ah) and 6 (ai) mice. Exact *P* values: (a) HUVEC *vs* lung ECs: 0.0278; HUVEC *vs* colon ECs: 0.1086; HUVEC *vs* liver ECs: 0.3334; HUVEC *vs* HEPG2: <0.0001; (f) <0.0001; (g) 0.3491; (h) <0.0001; (i) 0.8247; (l) 0.0012; (m) 0.050; (p) superficial: 0.1218; deep: 0.1720; (q) superficial: 0.9995; deep: 0.4289; (t) superficial: 0.9792; deep: 0.6602; (u) superficial: 0.7979; deep: 0.1275; (ad) 0.9021; (ae) 0.2279; (af) 0.7647; (ag) 0.3614. Scale bars are 200 μm in j-k, n-o and r-s, 20 μm in v-ac and 1 mm in ah-ai. HEPG2: hepatocellular carcinoma cells; mLiEC: mouse liver ECs; Tam: tamoxifen; lox: loxed allele; Δ: recombined allele; NG2: chondroitin sulfate proteoglycan 4; Edu: 5-ethynyl-2'-deoxyuridine. For gel source images, see Supplemental Information Fig. 1.

EXTENDED DATA FIGURE 2: EFFECTS OF SILENCING AND PHARMACOLOGICAL INHIBITION OF GS ON EC VIABILITY AND CENTRAL METABOLISM

a, *GS* mRNA levels in control ECs and ECs transduced with two different non-overlapping shRNAs targeting *GS* (GS^{KD1} and GS^{KD2}; GS^{KD1} is used in the experiments in the main manuscript and denoted as GS^{KD}) or transfected with scrambled siRNA (SCR) or siRNA targeting *GS* (siGS). Data are expressed as % of the respective control, denoted by the horizontal dotted line (mean±s.e.m.; n=28 independent experiments for GS^{KD1}, n=3

independent experiments for GS^{KD2} and n=9 independent experiments for siGS; *P<0.05 *vs* the respective control; one sample *t* test). **b-c,** Quantification of number of sprouts (b) and total sprout length (c) for spheroid sprouting assays with GS^{KD} ECs and GS^{KD} ECs expressing a shRNA-resistant *GS* mutant (rGS^{OE}) (mean±s.e.m.; n=3 independent experiments; *P<0.05 and ^{NS}P>0.05 *vs* control; ANOVA with Dunnett's multiple comparison *vs* control). **d,** Viability of control and GS^{KD} ECs as measured by lactate dehydrogenase (LDH) release assay (mean±s.e.m.; n=3 independent experiments; ^{NS}P>0.05 *vs* control, one sample *t* test). **e,** Intracellular reactive oxygen species (ROS) levels measured by CM-H_2DCFDA staining (mean±s.e.m.; n=3 independent experiments; ^{NS}P>0.05 *vs* control, Student's *t* test). **f,** Energy charge measurement (([ATP] + 1⁄2[ADP]) / ([ATP] + [ADP] + [AMP])) in GS^{KD} and control ECs (mean±s.e.m.; n=3 independent experiments; ^{NS}P>0.05 *vs* control, Student's *t* test). **g,** Ratio of oxidized glutathione over total glutathione levels (GSSG/(GSH+GSSG)) in GS^{KD} and control ECs (mean±s.e.m.; n=4 independent experiments; ^{NS}P>0.05 *vs* control, Student's *t* test). **h,** NADP/NADPH ratio in GS^{KD} and control ECs (mean±s.e.m.; n=5 independent experiments; ^{NS}P>0.05 *vs* control, one sample *t* test). **i-k,** Effect of GS^{KD} on major metabolic fluxes including glycolysis (i), glucose oxidation (j) and glutamine oxidation (k) (mean±s.e.m.; n=3 independent experiments for (i), n=5 for (j) and n=4 for (k); ^{NS}P>0.05 *vs* control, one sample *t* test). **l,m,** Oxygen consumption rate (OCR) in control, MSO-treated and GS^{KD} ECs in basal state and after injection of oligomycin, FCCP and antimycin A (l) (mean±s.e.m.; n=3 independent experiments), and calculation of OCR_{BAS}, OCR_{ATP} and maximal respiration (m) (mean±s.e.m.; n=3 independent experiments). Exact *P* values: (a) GS^{KD1}: <0.0001; GS^{KD2}: <0.0001; siGS: <0.0001; (b) ctrl *vs* GS^{KD}: 0.0147; ctrl *vs* GS^{KD} + rGS^{OE}: 0.9824; (c) ctrl *vs* GS^{KD}: 0.0083; ctrl *vs* GS^{KD} + rGS^{OE}: 0.6528; (d) 0.5717; (e) 0.8206 ; (f) 0.3715; (g) 0.4398; (h) 0.9291; (i) 0.4691 (j) 0.6643 (k) 0.6786. AU: arbitrary units; CM-DCF: 5-(and-6)-chloromethyl-2′,7′-dichlorodihydrofluorescein diacetate, acetyl ester; FCCP: carbonyl

cyanide-4-(trifluoromethoxy) phenylhydrazone; OCR_{BAS}: basal oxygen consumption rate; OCR_{ATP}: ATP-generating oxygen consumption rate; RFU: relative fluorescence units; MSO, methionine sulfoximine.

EXTENDED DATA FIGURE 3: *GS* KNOCK-DOWN REDUCES EC MOTILITY

a, Wound closure in control and GS^{KD2} EC monolayer scratch assays with or without MitoC-pretreatment (mean±s.e.m.; n=7 and 5 independent experiments for with and without MitoC respectively; $^{*}P<0.05$ *vs* corresponding control; Student's *t* test). **b,** Quantification of lamellipodial area (% of total cellular area) in control and GS^{KD2} ECs (mean±s.e.m.; n=3 independent experiments; $^{*}P<0.05$ *vs* control; Student's *t* test). **c,** Wound closure in monolayer scratch assays with SCR- and siGS-transfected ECs (mean±s.e.m.; n=5 independent experiments; $^{*}P<0.05$ *vs* SCR; Student's *t* test). **d,** Quantification of lamellipodial area (% of total cellular area) in SCR- and siGS-transfected ECs (mean±s.e.m.; n=5 independent experiments; $^{*}P<0.05$ *vs* SCR; Student's *t* test). **e,** [^{3}H]-Thymidine incorporation into DNA in SCR- and siGS-transfected ECs (mean±s.e.m.; n=3 independent experiments; $^{NS}P>0.05$ *vs* SCR; Student's *t* test). Exact *P* values: (a) ctrl *vs* GS^{KD2}: 0.0290; ctrl *vs* GS^{KD2} + MitoC: 0.0223; (b) 0.0088; (c) 0.0407; (d) 0.0083; (e) 0.4335.

EXTENDED DATA FIGURE 4: EFFECTS OF *GS* SILENCING ON CYTOSKELETON AND BARRIER FUNCTION

a-h, Images of control (a,c,e,g) and GS^{KD} (b,d,f,h) ECs after staining for α-tubulin (a,b), F-actin (c,d) and nuclear staining (e,f); images shown are representative for 3 independent experiments. **i-k,** Representative images of phalloidin + Hoechst-stained liver ECs 6 hours after isolation from control (i) and MSO-treated (j) mice, and corresponding quantification

of F-actin levels (k) (mean±s.e.m.; n=5 mice per group; **P*<0.05 *vs* control, Student's *t* test). **l-n,** Representative images of phalloidin-stained (F-actin) confluent monolayer control (l) and GS^{KD} (m) ECs aligning a scratch wound, and quantification of F-actin levels (n) (mean±s.e.m.; n=5 independent experiments; **P*<0.05 *vs* control, Student's *t* test). **o,** Quantification of the length of discontinuous and continuous VE-cadherin-stained junctions in control and GS^{KD} ECs (mean±s.e.m.; n=4 independent experiments; **P*<0.05 *vs* control, Student's *t* test). **p,** Quantification of VE-cadherin gap size index in control and GS^{KD} EC monolayers (mean±s.e.m.; n=4 independent experiments; **P*<0.05 *vs* control, Student's *t* test). **q-v,** Corresponding representative images of monolayer control and GS^{KD} ECs stained for VE-cadherin (q,r,u,v) and F-actin (s,t,u,v). Yellow arrows in (r) point to discontinuous VE-cadherin junctions and yellow asterisks indicate intracellular gaps. **w,** Quantification of transendothelial electrical resistance (TEER) in control and GS^{KD} EC monolayers (mean±s.e.m.; n=4 independent experiments; **P*<0.05 *vs* control, Student's *t* test at each time point). **x-z,** Quantification (x) of Evans blue dye extracted from the ears of control and MSO-treated mice induced by topical application of mustard oil (n=4 mice for each condition, **P*<0.05; Student's *t* test) and representative pictures of the Evans blue leakage into the ear tissue in control (y) and MSO-treated (z) mice. Exact *P* values: (k) 0.0030; (n) 0.0036; (o) continuous ctrl *vs* GS^{KD}: 0.0005; discontinuous ctrl *vs* GS^{KD}: 0.0005; (p) 0.0356; (w) 0.0181; (x) 0.0002. Scale bar is 20 μm in a-h and in l-m and 10 μm in i-j and in q-v. AU: arbitrary units.

EXTENDED DATA FIGURE 5: ENZYMATIC ACTIVITY OF GS AND ITS ROLE IN EC MIGRATION

a, Scheme of $^{15}NH_4^+$ labeling of glutamate and glutamine with unlabeled carbons (blue) and labeled nitrogens (red). **b,** ^{15}N incorporation into glutamine (% isotope enrichment in m+1 and m+2, 30 min after adding $^{15}NH_4^+$) in medium with dialyzed serum and different glutamine concentrations (mean±s.e.m.; n=3 independent experiments; ANOVA with

Dunnett's multiple comparisons *vs* 4 mM; **P* <0.05). **c,** ^{15}N incorporation into glutamate (% isotope enrichment in m+1) and glutamine (% isotope enrichment in m+1 and m+2), 30 min after adding increasing concentrations of $^{15}NH_4Cl$ (mean±s.e.m.; n=3 independent experiments). **d,** Scheme of glutamine labeling from [U-^{13}C]-glutamate with unlabeled nitrogens (blue) and labeled carbons (red). **e,** Label contribution of [U-^{13}C]-glutamate to intracellular glutamine at various glutamine concentrations (% isotope enrichment in glutamine and glutamate m+5, 30 min after adding the tracer) (mean±s.e.m.; n=3 independent experiments; ANOVA with Dunnett's multiple comparisons *vs* 4 mM; **P* <0.05). **f,** Scheme for [U-^{13}C]-glucose carbon contribution to glutamine with labeled carbons (red) and unlabeled carbons (blue). Incorporation is shown after one turn of the TCA cycle. **g,** Total contribution of [U-^{13}C]-glucose carbons to α-ketoglutarate, glutamate and glutamine in ECs in medium with or without glutamine, 48 h after adding the tracer (mean±s.e.m.; n=3 independent experiments; **P*<0.05 *vs* total contribution in Gln at 0.6 mM external Gln, ANOVA with Dunnett's multiple comparisons). **h,** ^{15}N incorporation into glutamine (% isotope enrichment in m+1 and m+2, 30 min after adding $^{15}NH_4^+$) in ECs and HEPG2 cells (mean±s.e.m.; n=4 independent experiments (ND=not detected)). **i,** ^{13}C-glutamine uptake kinetics in control, MSO-treated and GS^{KD} ECs and subsequent conversion to glutamate. See Methods for explanation of the different time points. Data are expressed as m+5 isotopomer, as percentage of the total intracellular glutamine (gln) or glutamate (glu) pool (mean±s.e.m.; n=3 independent experiments, except for 30 min where n=1 experiment; no statistical differences between control, MSO-treated and GS^{KD} were observed for glutamine nor for glutamate; ANOVA with Dunnett's multiple comparison *vs* control at each time point; no statistical analysis was performed at 30 min). **j,** ^{14}C-glutamine uptake in control and GS^{KD} ECs (mean±s.e.m.; n=5 independent experiments; ^{NS}P>0.05 *vs* control, one sample *t* test). **k,** Ratio of intracellular glutamine (Gln) over glutamate (Glu) levels in control and GS^{KD} ECs (mean±s.e.m.; n=3 independent

experiments; ^{NS}P>0.05 *vs* control, Student's *t* test). **l,** Velocity measurement of control and GS^{KD} ECs at different glutamine (Gln) concentrations (mean±s.e.m.; n=4 independent experiments; *P<0.05 *vs* corresponding control, mixed models R statistics). **m-n,** Effect of glutamine concentration on sprout number (m) and total sprout length (n) in control and GS^{KD} spheroids (mean±s.e.m.; n=3 independent experiments; *P <0.05 *vs* corresponding control, mixed models R statistics). **o-p,** Number of sprouts per spheroid (o) and total sprout length (p) in control and MSO-treated EC spheroids (mean±s.e.m.; n=3 independent experiments; *P<0.05 *vs* control, paired Student's *t* test). **q-s,** Effect of MSO-treatment on EC motility parameters: wound closure of MitoC-treated ECs (q) (mean±s.e.m.; n=11 independent experiments; *P<0.05 *vs* control, Student's *t* test), lamellipodial area (r) (mean±s.e.m.; n=10 independent experiments; *P<0.05 *vs* control, paired Student's *t* test) and F-actin levels, 1 h after latrunculin wash-out (s) (mean±s.e.m.; n=4 independent experiments; *P<0.05 *vs* control, one-sample *t* test). **t,** [^{3}H]-Thymidine incorporation in control and MSO-treated ECs (mean±s.e.m.; n=3 independent experiments; ^{NS}P>0.05 *vs* control, one sample *t* test). Exact *P* values: (b) m+1 0.025 mM *vs* m+1 4 mM: 0.0096; m+1 0.6 mM *vs* m+1 4 mM: 0.1206; m+2 0.025 mM *vs* m+2 4 mM: 0.0839; m+2 0.6 mM *vs* m+2 4 mM: 0.9921; (e) Glu m+5 0.6 mM *vs* Glu m+5 4 mM: 0.9372; Glu m+5 0.025 mM + MSO *vs* Glu m+5 4 mM: 0.0034; Glu m+5 0.025 mM *vs* Glu m+5 4 mM: 0.0215; Gln m+5 0.6 mM *vs* Gln m+5 4 mM: 0.9297; Gln m+5 0.025 mM + MSO *vs* Gln m+5 4 mM: 0.9961; Gln m+5 0.025 mM *vs* Gln m+5 4 mM: 0.0268; (g) α-keto 0.6 mM *vs* Gln 0.6 mM: 0.0001; Glu 0.6 mM *vs* Gln 0.6 mM: 0.0001; Gln 0 mM *vs* Gln 0.6 mM: 0.0285; (i) Gln 0.5 min: ctrl *vs* MSO: 0.4846; ctrl *vs* GS^{KD}: 0.5904; Gln 10 min: ctrl *vs* MSO: 0.6709; ctrl *vs* GS^{KD}: 0.6910; Gln 20 min: ctrl *vs* MSO: 0.5896; ctrl *vs* GS^{KD}: 0.6784; Glu 0.5 min: ctrl *vs* MSO: 0.9774; ctrl *vs* GS^{KD}: 0.8810; Glu 10 min: ctrl *vs* MSO: 0.0502; ctrl *vs* GS^{KD}: 0.9598; Glu 20 min: ctrl *vs* MSO: 0.9782; ctrl *vs* GS^{KD}: 0.7783. (j) 0.6623; (k) 0.6704; (l) ctrl *vs* GS^{KD} 0.1 mM: 0.0054; ctrl *vs* GS^{KD} 0.6 mM: 0.0247 ctrl *vs* GS^{KD} 2 mM:

0.0017; (m) ctrl *vs* GS^{KD} 0.6 mM and 10 mM: < 0.0001; (n) ctrl *vs* GS^{KD} 0.6 mM and 10 mM: < 0.0001; (o) 0.0313; (p) 0.0075; (q) 0.0019; (r) 0.0116; (s) 0.0091; (t) 0.5110. α-keto: α-ketoglutarate; GDH: glutamate dehydrogenase; Glu: glutamate; GS: glutamine synthetase; Gln: glutamine; MSO, methionine sulfoximine; MitoC: mitomycin C.

EXTENDED DATA FIGURE 6: RESCUING THE GS^{KD} PHENOTYPE *IN VITRO*

a, Schematic representation of the DORA RHOA FRET biosensor, depicting from N- to C-terminal the circular permutated RHOA effector protein kinase N (cpPKN), the dimeric circular permutated Venus (dcpVen), the ribosomal protein-based linkers (L9), the dimeric Cerulean3 (dCer3) and RHOA. **b-m,** Representative images of control (b-d), MSO-treated (e-g), GS^{KD} (h-j) and $RHOJ^{KD}$ (k-m) ECs after staining for F-actin (phalloidin) (b,d,e,g,h,j,k,m) and pMLC (c,d,f,g,i,j,l,m). **n,** Quantification of the pMLC-immunoreactivity (mean±s.e.m.; n=5 independent experiments; $^{*}P<0.05$ *vs* control, one sample *t* test). **o-t,** Representative images of control (o,q,s) and GS^{KD} (p,r,t) EC spheroids treated with vehicle (o,p) or the ROCK inhibitors Y27632 (q,r) or fasudil hydrochloride (s,t). **u-v,** Quantification of the number of sprouts per spheroid (u) and sprout length (v) (mean±s.e.m.; n=3 independent experiments; $^{*}P<0.05$ and $^{NS}P>0.05$ *vs* untreated control, ANOVA with Dunnett's multiple comparisons *vs* untreated control). **w,** Quantification of the lamellipodial area in vehicle- or fasudil hydrochloride-treated control and GS^{KD} ECs (mean±s.e.m.; n=6 independent experiments; $^{*}P<0.05$ and $^{NS}P>0.05$ *vs* untreated control, ANOVA with Dunnett's multiple comparisons *vs* untreated control). **x,** Quantification of the lamellipodial area in vehicle-, ML7- or peptide 18-treated GS^{KD} and control ECs (mean±s.e.m.; n=4 independent experiments of which 3 experiments included the ML7-treatment; $^{*}P<0.05$ *vs* untreated control, ANOVA with Dunnett's multiple comparisons *vs* untreated control). **y,** Scratch wound closure in vehicle-, ML7- or peptide 18-treated GS^{KD} and control ECs (mean±s.e.m.; n=3 independent experiments; $^{*}P<0.05$ *vs* untreated control, ANOVA with

Dunnett's multiple comparisons *vs* untreated control). **z,** Fold-changes (*vs* untreated control ECs) in F-actin levels from phalloidin-stained vehicle-, ML7- or peptide 18-treated GS^{KD} ECs (mean±s.e.m.; n=4 independent experiments of which 3 included the peptide 18-treatment; *P<0.05 *vs* untreated control, one sample *t* test). **aa,** Fold-changes (*vs* untreated control ECs) in pMLC levels from pMLC-immunostained vehicle-, ML7- or peptide 18-treated GS^{KD} ECs (mean±s.e.m.; n=4 independent experiments of which 3 included the peptide 18-treatment; *P<0.05 *vs* untreated control, one sample *t* test. Exact *P* values: (n) MSO: 0.0372; GS^{KD}: 0.0060; $RHOJ^{KD}$: 0.0051; (u) GS^{KD} *vs* ctrl: 0.0045; Fasu *vs* ctrl: 0.9596; GS^{KD} + Fasu *vs* ctrl: 0.8857; (v) GS^{KD} *vs* ctrl: 0.0199; Fasu *vs* ctrl: 0.8309; GS^{KD} + Fasu *vs* ctrl: 0.9327; (w) GS^{KD} *vs* ctrl: 0.0074; Fasu *vs* ctrl: 0.5906; GS^{KD} + Fasu *vs* ctrl: 0.9900; (x) GS^{KD} *vs* ctrl: 0.0011; GS^{KD} + ML7 *vs* ctrl: 0.0079; GS^{KD} + pep.18 *vs* ctrl: 0.0017; (y) GS^{KD} *vs* ctrl: 0.0034; GS^{KD} + ML7 *vs* ctrl: 0.0022; GS^{KD} + pep.18 *vs* ctrl: 0.0040; (z) GS^{KD}: 0.0058; ML7: 0.0072; pep.18: 0.0888; (aa) GS^{KD}: 0.0369; ML7: 0.0021; pep.18: 0.1672. Fasu., fasudil hydrochloride; pep. 18, peptide 18. Scale bar is 20 μm in (b-m) and 100 μm in (o-t). For gel source images, see Supplemental Information Fig. 1.

EXTENDED DATA FIGURE 7: RHOGTPASE LOCALIZATION AND INTERACTION WITH GS

a, Co-IP assays showing no detectable interaction between GS and RHOA or RHOC (red asterisk indicates a non-specific band (also present in the IgG controls and unaffected by silencing of RHOA or RHOC). Picture shown is representative for 3 independent experiments. **b,** Co-IP of overexpressed GS and RHOJ-EGFP or ΔN-RHOJ-EGFP in ECs. Quantifications are mean±s.e.m.; n=4 independent experiments; *P<0.05, one-sample *t* test. In some of the experiments, the expression of ΔN20-RHOJ-EGFP was lower than expression of RHOJ-EGFP. To correct for this, densitometric quantification was performed and signals in IP lanes were normalized to input signals. **c,** Immunoblotting for RHOA and RHOC on cytosolic (c) and membrane (m) fractions of ECs with NaK as membrane marker

and GAPDH as cytosolic marker. Picture shown is representative for 3 independent experiments. **d,** Bimolecular fluorescence complementation (BiFC) assay with GS coupled to the N-terminal half of EGFP, and RHOJ coupled to the C-terminal half of EGFP. Only when GS and RHOJ are in close proximity, the two EGFP half-sites complement each other and form a functional EGFP. **e,** Percentage of ECs displaying BiFC upon overexpression of GS-EGFP$^{1/2}$ and RHOJ-EGFP$^{2/2}$ or GS-EGFP$^{1/2}$ and ΔN-RHOJ-EGFP$^{2/2}$. Data are mean±s.e.m.; n=3 independent experiments; **P*<0.05; Student's *t* test. **f,** Scheme for SPT-PALM imaging under TIRF illumination with the plasma membrane depicted at the top. The TIRF region is bright (whereas the part outside the TIRF region is grayed out) and contains the plasma membrane and its immediately adjacent space (not shown at exact relative dimensions). Weight and number of arrowheads represent velocity of single particles (the photoswitchable fluorescent protein (PSFP) or the PSFP coupled to the protein of interest (here GS)). The PSFP is activated upon entry into the TIRF region and is color-coded differently inside *vs* outside of the TIRF region. PSFP-GS displays reduced velocity in the TIRF region, presumably because of palmitoylation and membrane association of GS. **g,** Scheme for in-cell labeling of proteins with clickable alkyne-containing palmitoylation probes and subsequent biotin-azide clicking. X represents a palmitoylated protein, N_3 is the biotin-coupled azide. **h-i,** Rate of CoA release from palmitoyl-CoA as readout for recombinant human GS autopalmitoylation while varying either the doses of palmitoyl-CoA (h) or the amounts of recombinant GS (i) (mean±s.e.m.; n=4 independent experiments for h and n=5 for i; **P*<0.05, ANOVA with Dunnett's multiple comparisons *vs* 0 μM palmitoyl-CoA or *vs* 0.5 μg recombinant GS). **j**, Representative GS immunoblot (of 3 independent experiments) for binding of recombinant human GS to palmitoyl-CoA agarose. IF=input fraction; FT=flow through; W8=wash fraction 8; SDS=eluate. **k-m,** Representative images of RHOJ-EGFP localization in ECs under vehicle-treatment (k) or treatment with 2BP (pan-palmitoylation inhibitor) (l). Red

arrowheads indicate EGFP signal at membrane ruffles, which was quantified as percent of total cellular area (m) (mean±s.e.m.; n=4 independent experiments; *P<0.05 *vs* vehicle-treated, paired Student's *t* test). **n-p,** Representative images of ECs overexpressing wt RHOJ-EGFP (n), RHOJ-EGFP point-mutated on cysteine residue 3 (C3A) (o) or RHOJ-EGFP point-mutated on cysteine residue 11 (C11A) (p). Red arrowheads indicate RHOJ at the plasma membrane. ECs that are not completely in the field of view have been masked out in blue. **q**, Quantification of the RHOJ-EGFP positive area at the plasma membrane as a percentage of total cell area. Data are mean±s.e.m.; n=5 independent experiments; *P<0.05; ANOVA with Dunnett's comparison *vs* wt RHOJ. **r**, RHOJ immunoblotting on membrane *vs* cytosolic fractions from ECs overexpressing wt RHOJ-EGFP (RHOJ WT), RHOJ-EGFP point-mutated on cysteine residue 3 (RHOJ C3A) or RHOJ-EGFP point-mutated on cysteine residue 11 (RHOJ C11A), with NaK as membrane marker and GAPDH and α-tubulin as cytosolic markers. **s**, Densitometric quantification of RHOJ/NaK as determined in (r). Data are mean±s.e.m.; n=6 independent experiments; *P<0.05; one sample *t* test. **t,** RHOJ activity in ECs under vehicle- or 2BP-treatment (blots are representative of 3 independent experiments; densitometric quantification in arbitrary units (AU) is mean±s.e.m; *P<0.05, paired Student's *t* test *vs* vehicle-treated). **u,** RHOJ immunoblotting for control and GS^{KD} ECs overexpressing RHOJ ($RHOJ^{OE}$) subjected to acyl-RAC. The cleaved bound fraction (cBF) represents palmitoylated RHOJ. IF is the input fraction, whereas the cleaved unbound fraction (cUF) and the preserved bound fraction (pBF) are controls showing depletion of RHOJ from the thioester cleaving reagent and near absence of non-specific binding of RHOJ to the resin (see Methods). Densitometric quantification of cBF/IF is shown (mean±s.e.m; n=3 independent experiments; *P<0.05, one-sample *t* test *vs* control). **v,** GRAPHICAL ABSTRACT: *Left side:* Autopalmitoylation allows endothelial GS to interact directly (or indirectly) with the RhoGTPase RHOJ and to sustain RHOJ's palmitoylation, membrane localization and

activity (reflected by GTP binding). RHOJ activity then sustains normal EC migration and lamellipodia formation, and keeps actin stress fiber formation at levels, promoting normal EC migration and vessel branching *in vivo*. Through mechanisms that are incompletely understood, active RHOJ inhibits signaling of the RHOA/B/C – ROCK – (p)MLC pathway (itself known to promote stress fiber formation). The relative contribution of a direct effect of RHOJ on migration *vs* the indirect effect through RHOA/B/C – ROCK – (p)MLC remains to be determined. Reduced opacity of RHOA/B/C, ROCK and (p)MLC indicates reduced signaling of this pathway. GTP: guanosine triphosphate. *Right side*: Loss of endothelial GS renders RHOJ less active (visually reflected by fewer palmitoylated, membrane-bound RHOJ proteins), and weakens the brake on the RHOA/B/C – ROCK – (p)MLC pathway. The resulting excessive stress fiber formation causes ECs to lose migratory capacity and reduces vessel branching *in vivo*. Dashed lines indicate reduced activity; red X indicates GS blockade; question mark indicates unknown mechanisms. Exact *P* values: (b) 0.0153; (e) 0.0334; (h) 2 *vs* 0 μM: 0.6327; 5 *vs* 0 μM: 0.2841; 10 *vs* 0 μM: 0.1090; 20 *vs* 0 μM: 0.0339; 40 *vs* 0 μM: 0.0034; (i) 1 *vs* 0.5 μg: 0.5806; 2 *vs* 0.5 μg: 0.0319; 4 *vs* 0.5 μg :0.0037; 8 *vs* 0.5 μg: 0.0001; 16 *vs* 0.5 μg: 0.0001; (m) 0.0313; (q) RHOJ C3A *vs* RHOJ WT: 0.0001; RHOJ C11A *vs* RHOJ WT: 0.0001; (s) RHOJ C3A *vs* RHOJ WT: 0.0015; RHOJ C11A *vs* RHOJ WT: 0.0007; (t) 0.0051; (u) 0.0461. Scale bar is 200 μm in k,l,n-p. For gel source images, see Supplemental Information Fig. 1.

EXTENDED DATA FIGURE 8: POSSIBLE MOLECULAR MODEL OF GS AUTOPALMITOYLATION

a. Structure of human GS and of its bifunnel-shaped catalytic site. Schematic representation of the GS decamer in top and front view with individual subunits A and B labeled and colored gray and green, respectively. Close-up of the bifunnel catalytic site which is formed between subunits A and B. The GS decamer has 10 active sites, each located at the interface of two adjacent subunits. ATP enters from the top whereas

glutamate enters from below; Manganese ions (Mn^{2+}) are shown as metalic spheres. **b.** Molecular dynamics (MD) simulation of palmitoyl-CoA in the catalytic cleft of GS predicts that, while the head of palmitoyl-CoA is tightly bound to the adenine binding site, the tail can point in opposing directions with respect to the protein's principal axis. The most representative structures of the two alternative poses observed during the long MD simulations for palmitoyl-CoA binding to GS (in blue, seen from two different perspectives) are shown in red (A, tail bending upwards) and green (B, tail bending downwards). **c.** Detailed view on the main conformation – conformation A – is shown in more details. The sulfur atom of palmitoyl-CoA (which is immediately adjacent to the carbon on which the nucleophilic attack occurs) (colored yellow) approaches the highly conserved C209 (also colored yellow), with an interatomic distance (S-S) that during the simulations reversibly fluctuates between 3 and 8 Å. The hydrophobic tail positions itself along grooves characterized by the presence of hydrophobic residues. Color coding: carbons are grey, nitrogens blue, phosphorous golden and oxygens red. Cysteines and serines within 5 Å from the palmitoyl tail are highlighted in yellow and orange, respectively. The hydrophobic residues around the tail are shown in green. **d.** Detailed view on conformation B where the tail is found in a buried hydrophobic cleft, with the sulfur at a distance of 5 Å or less from the conserved serines 65 and 75 and the tail occupying the site of the GS inhibitor MSO. Details are shown of the extensive steric clash between MSO and the secondary binding pose (B) observed in palmitoyl-CoA MD simulations. Palmitoyl-CoA is represented as sticks with standard atomic colours. MSO is shown in cyan and its position is taken from the 2QC8 entry in the protein databank. Cysteines and serines within 5 Å from the palmitoyl tail are highlighted in yellow and orange, respectively. The hydrophobic residues around the tail are shown in green. **e.** GS immunoblotting after streptavidin pull-down of biotin-azide clicked lysates from 16C-YA (palmitoylation probe) labeled HEK-293T cells overexpressing wild type *GS* or *GS* point-mutated for C209. The input shows the level of

GS overexpression. Representative blot for 4 independent experiments is shown. **f-g.** Quantification of total sprout length (f) and number of sprouts per spheroid (g) for control and GS^{KD} ECs with or without overexpression of shRNA resistant C209A-point mutated *GS* ($rGS^{C209A\text{-}OE}$) (mean ± s.e.m.; n=4 independent experiments; $*P < 0.05$ *vs* control, ANOVA with Dunnett's multiple comparison *vs* control). **h.** Schematic representation of protein autopalmitoylation. Upon binding of palmitoyl-CoA to the protein, free CoA (gray oval) is released and can be detected. **i.** Recombinant wild-type (WT) and point-mutated (R324C and R341C) GS were incubated with different doses of palmitoyl-CoA in a cell-free system at physiologcial pH. Release of CoA per minute was determined as a direct readout for protein autopalmitoylation. Data are mean ± s.e.m. of 3 (R324C and R341C) and 4 (WT) independent experiments. $^{NS}P>0.05$; $*P<0.05$ according to two way ANOVA comparing the entire dose-response to the dose-response of WT GS. **j.** Different amounts of recombinant WT, R324C and R341C GS were incubated with a fixed amount of palmitoyl-CoA (40 µM) and CoA release per minute was determined as readout for autopalmitoylation. Data are mean ± s.e.m. of 4 (R324C and R341C) and 5 (WT) independent experiments. $^{NS}P>0.05$; $*P<0.05$ according to two way ANOVA comparing the entire dose-response to the dose-response of WT GS. The data for WT GS from panels (i) and (j) are also included in Extended Data Fig. 7 as stand-alone data, but are included here too for comparison purposes. **k.** Boyden chamber migration for control, GS^{KD}, GS^{KD} + rGS^{OE} (r = shRNA-resistant; OE = overexpression), GS^{KD} + $rGS^{R341C\text{-}OE}$ and GS^{KD} + $rGS^{R324C\text{-}OE}$ ECs, all under mitomycin C-treatment (mean ± s.e.m.; n=3 independent experiments; $^{NS}P>0.05$; $*P<0.05$, ANOVA with Dunnett's multiple comparison *vs* control). Exact *P* values: (f) GS^{KD} *vs* ctrl: 0.0004; GS^{KD} + $rGS^{C209A\text{-}OE}$ *vs* ctrl: 0.0004; (g) GS^{KD} *vs* ctrl: 0.0001; GS^{KD} + $rGS^{C209A\text{-}OE}$ *vs* ctrl: 0.0001; (i) R324C *vs* WT: 0.8228; R341C *vs* WT: 0.7530; (j) R324C *vs* WT: 0.1331; R341C *vs* WT: 0.0003; (k) GS^{KD} *vs* ctrl: 0.0054; GS^{KD} +

1744 rGS^{OE} *vs* ctrl: 0.8152; GS^{KD} + $rGS^{R341C-OE}$ *vs* ctrl: 0.3645; GS^{KD} + $rGS^{R324C-OE}$ *vs* ctrl:
1745 0.2118. For gel source images, see Supplemental Information Fig. 1.

1746

1747

1748

1749

1750

1751

1752

1753

1754

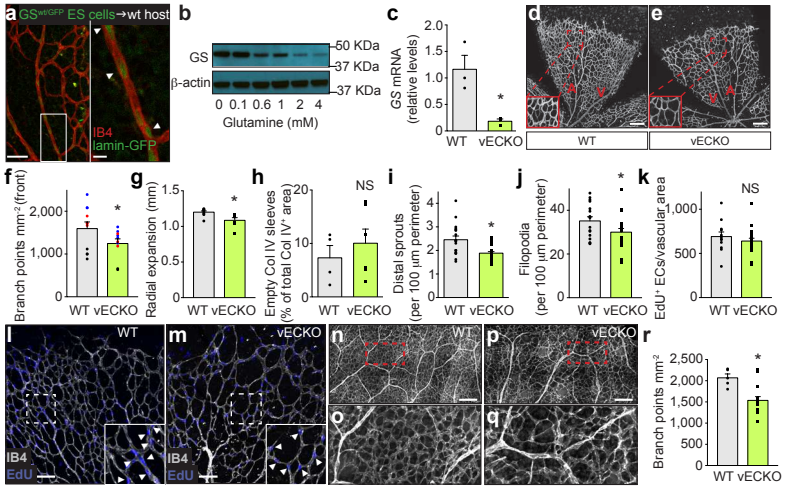
a
GSwtGFP ES cells→wt host
IB4
lamin-GFP
b
GS
β-actin
50 KDa
37 KDa
37 KDa
0 0.1 0.6 1 2 4
Glutamine (mM)
c
GS mRNA (relative levels)
WT vECKO
d
e
WT
vECKO
f
Branch points mm-2 (front)
WT vECKO
g
Radial expansion (mm)
WT vECKO
h
Empty Col IV sleeves (% of total Col IV+ area)
NS
WT vECKO
i
Distal sprouts (per 100 µm perimeter)
WT vECKO
j
Filopodia (per 100 µm perimeter)
WT vECKO
k
EdU+ ECs/vascular area
NS
WT vECKO
l
WT
IB4
EdU
m
vECKO
IB4
EdU
n
WT
o
p
vECKO
q
r
Branch points mm-2
WT vECKO

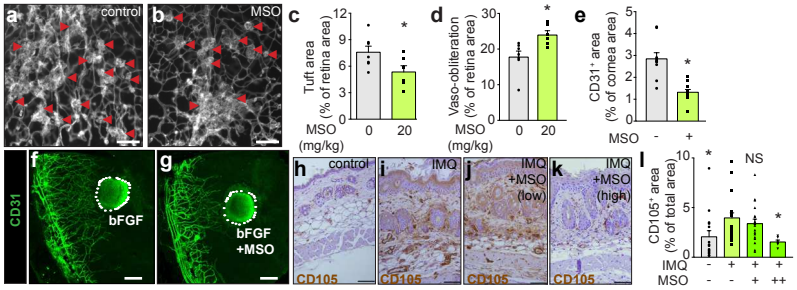
a
control
b
MSO
c
Tuft area
(% of retina area)
MSO
(mg/kg)
0
20
d
Vaso-obliteration
(% of retina area)
e
CD31+ area
(% of cornea area)
MSO
-
+

CD31
f
bFGF
g
bFGF
+MSO
h
control
i
IMQ
j
IMQ
+MSO
(low)
k
IMQ
+MSO
(high)
CD105
l
CD105+ area
(% of total area)
NS
IMQ
MSO

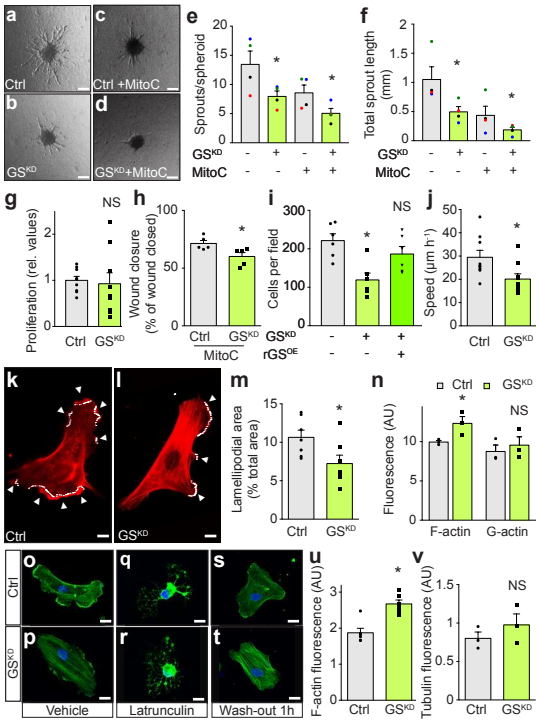
a
Ctrl
b
GSKD
c
Ctrl +MitoC
d
GSKD+MitoC
e
Sprouts/spheroid
GSKD
MitoC
f
Total sprout length (mm)
GSKD
MitoC
g
Proliferation (rel. values)
NS
Ctrl
GSKD
h
Wound closure (% of wound closed)
Ctrl
GSKD
MitoC
i
Cells per field
NS
GSKD
rGSOE
j
Speed (μm h-1)
Ctrl
GSKD
k
Ctrl
l
GSKD
m
Lamellipodial area (% total area)
Ctrl
GSKD
n
Ctrl
GSKD
Fluorescence (AU)
NS
F-actin
G-actin
o
p
q
r
s
t
Ctrl
GSKD
Vehicle
Latrunculin
Wash-out 1h
u
F-actin fluorescence (AU)
Ctrl
GSKD
v
Tubulin fluorescence (AU)
NS
Ctrl
GSKD

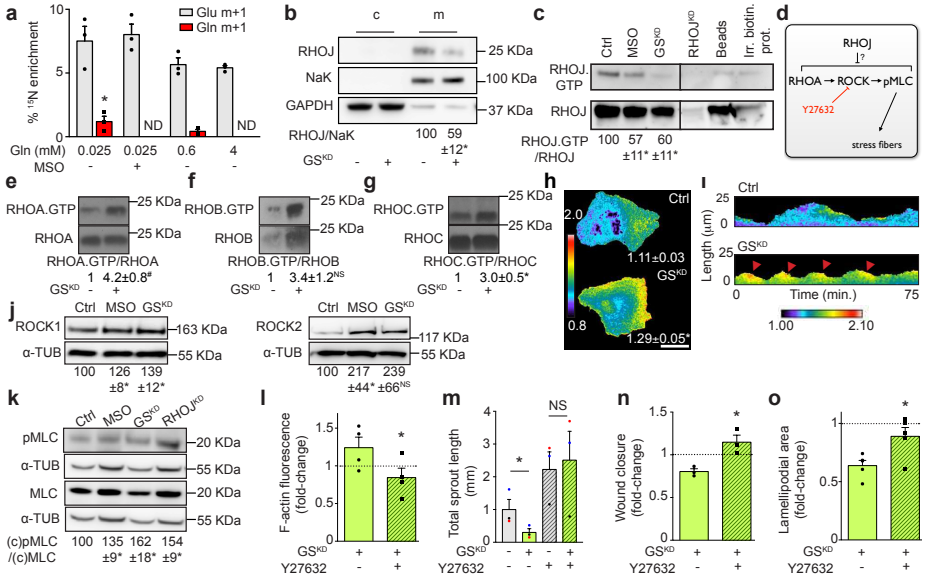
a
% 15N enrichment
Glu m+1
Gln m+1
ND
ND
Gln (mM) 0.025 0.025 0.6 4
MSO - + - -
b
c
m
RHOJ
NaK
GAPDH
25 KDa
100 KDa
37 KDa
RHOJ/NaK 100 59 ±12*
GSKD - + - +
c
Ctrl
MSO
GSKD
RHOJKD
Beads
Irr. biotin. prot.
RHOJ.GTP
RHOJ
RHOJ.GTP /RHOJ 100 57 60 ±11* ±11*
d
RHOJ
1?
RHOA → ROCK → pMLC
Y27632
stress fibers
e
RHOA.GTP
RHOA
25 KDa
25 KDa
RHOA.GTP/RHOA
1 4.2±0.8#
GSKD - +
f
RHOB.GTP
RHOB
25 KDa
25 KDa
RHOB.GTP/RHOB
1 3.4±1.2NS
GSKD - +
g
RHOC.GTP
RHOC
25 KDa
25 KDa
RHOC.GTP/RHOC
1 3.0±0.5*
GSKD - +
h
Ctrl
2.0
1.11±0.03
GSKD
0.8
1.29±0.05*
i
Ctrl
25
0
GSKD
25
0
Length (µm)
0
Time (min.)
75
1.00
2.10
j
Ctrl MSO GSKD
ROCK1
α-TUB
163 KDa
55 KDa
100 126 139
±8* ±12*
Ctrl MSO GSKD
ROCK2
α-TUB
117 KDa
55 KDa
100 217 239
±44* ±66NS
k
Ctrl
MSO
GSKD
RHOJKD
pMLC
α-TUB
MLC
α-TUB
20 KDa
55 KDa
20 KDa
55 KDa
(c)pMLC /(c)MLC 100 135 162 154
±9* ±18* ±9*
l
F-actin fluorescence (fold-change)
GSKD + +
Y27632 - +
m
Total sprout length (mm)
NS
GSKD - + - +
Y27632 - - + +
n
Wound closure (fold-change)
GSKD + +
Y27632 - +
o
Lamellipodial area (fold-change)
GSKD + +
Y27632 - +

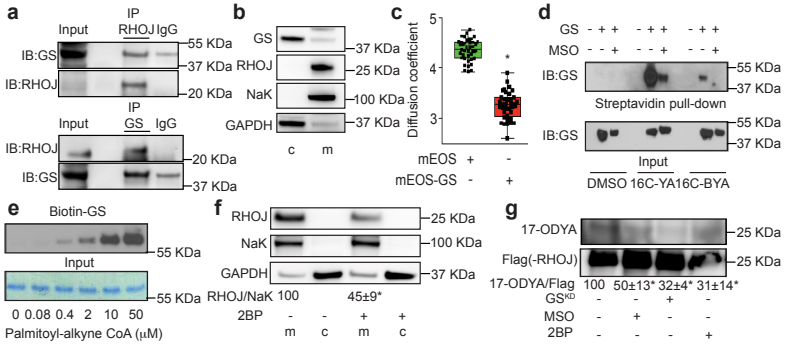
a
Input
IP
RHOJ
IgG
IB:GS
IB:RHOJ
55 KDa
37 KDa
20 KDa
Input
IP
GS
IgG
IB:RHOJ
IB:GS
20 KDa
37 KDa
b
GS
RHOJ
NaK
GAPDH
37 KDa
25 KDa
100 KDa
37 KDa
c
m
c
Diffusion coefficient
5
4
3
mEOS + -
mEOS-GS - +
d
GS - + + - + + - + +
MSO - - + - - + - - +
IB:GS
55 KDa
37 KDa
Streptavidin pull-down
IB:GS
55 KDa
37 KDa
Input
DMSO 16C-YA16C-BYA
e
Biotin-GS
55 KDa
Input
55 KDa
0 0.08 0.4 2 10 50
Palmitoyl-alkyne CoA (μM)
f
RHOJ
NaK
GAPDH
25 KDa
100 KDa
37 KDa
RHOJ/NaK 100 45±9*
2BP - - + +
m c m c
g
17-ODYA
Flag(-RHOJ)
25 KDa
25 KDa
17-ODYA/Flag 100 50±13* 32±4* 31±14*
GSKD - - + -
MSO - + - -
2BP - - - +